

Chapter 2

MEMS Technologies for Energy Harvesting

Manuel Domínguez-Pumar, Joan Pons-Nin and Juan Chávez

Abstract The objective of this chapter is to introduce the technology of Microelectromechanical Systems, MEMS, and its application to emerging energy harvesting devices. The chapter begins with a general introduction to the most common MEMS fabrication processes. Next, the chapter follows with a survey of design mechanisms implemented in MEMS energy harvesters to provide nonlinear mechanical actuations. Mechanisms to produce bistable potential will be studied, such as by placing fixed magnets, buckling of beams, or by using slightly slanted clamped-clamped beams. Other nonlinear mechanisms are studied such as impact energy transfer, or the design of nonlinear springs. Finally, due to their importance in the field of MEMS and their application to energy harvesters, an introduction to the actuation with piezoelectric materials is made. Examples of energy harvesters found in the literature using this actuation principle are also presented.

1 Introduction

The technology of Micro Electro Mechanical Systems, or MEMS, is generally defined as the miniaturization of mechanical and electro-mechanical structures that are fabricated using standard processes from the integrated circuit industry and other compatible processes usually aimed at 'sculpting' 3D structures. MEMS can in particular include moveable parts such as cantilevers, beams, membranes, plates, etc.

Manuel Domínguez-Pumar
MNT-DEE, Technical University of Catalonia (Barcelona), e-mail: manuel.dominguez@upc.edu

Joan Pons-Nin
MNT-DEE, Technical University of Catalonia (Barcelona), e-mail: joan.pons@upc.edu

Juan Chávez
GSS-DEE, Technical University of Catalonia (Barcelona), e-mail: juan.antonio.chavez@upc.edu

They may present interactions with biological, chemical and thermal phenomena, including the interaction with fluids. At the same time these devices usually interact with fields and forces that are not electromagnetic, such as mechanical forces, piezoelectric and thermoelectric forces, among others. This has promoted MEMS technology to be an excellent tool for the miniaturization of energy harvesters.

The usual physical dimensions of MEMS can range from below $1\mu\text{m}$ (in this case they are usually called Nano Electro Mechanical Systems), to the mm scale. It is remarkable that most times the MEMS equivalent of a sensors/actuator macrosystem outperforms the latter. Among other factors, the repeatability and high reliability of MEMS batch fabrication processes can clearly contribute to this improvement, while at the same time even reducing the unit cost. Furthermore, the recent merging between MEMS and CMOS technology has also opened new venues on which both the microelectromechanical parts and the sensing/actuation circuits can be found within the same silicon die.

This chapter is divided in three main parts. Section 2 will introduce the most common fabrication processes used in MEMS technology. Special attention will be paid to those processes that are specific to MEMS such as anisotropic etching. Section 3 will introduce the main design procedures that have been used in MEMS to generate nonlinear actuation and sensing in energy harvesters. In particular the creation of bistable potentials, impact energy transfer and nonlinear springs will be addressed. Recent examples found in the literature will be presented and linked with the fabrication of the devices. Finally, due to its growing relevance, in Section 5 an introduction to piezoelectricity will be made, presenting some examples also found in the literature of energy harvesters designed using piezoelectric actuation and sensing.

2 MEMS fabrication processes

This section provides a brief guide to the fabrication processes used in MEMS technology. Since MEMS fabrication developed out of Integrated Circuits (IC) fabrication, we focus first on the main differences between MEMS and IC technologies. It follows a description of the deposition and etching techniques most frequently used for MEMS, with special emphasis in those that are MEMS-specific, such as anisotropic etching, wafer bonding, and, in particular, Deep Reactive Ion Etching. The next focus is on MEMS fabrication strategies, including surface micromachining, bulk micromachining and Silicon On Insulator (SOI) based techniques. Finally, it is provided an example of a commercial process aimed at the fabrication of piezoelectric MEMS devices that can be suitable, among others, for energy harvesting applications.

2.1 IC versus MEMS fabrication

IC and MEMS fabrication possess in common a series of step processes (e.g. photolithography, etch, oxidation, diffusion, LPCVD or sputter deposition) and materials (e.g. silicon, polysilicon, silicon nitride, silicon oxide or metals). In fact, IC and MEMS fabrication technologies can be seen as a complex sequence of deposition, material growth, lithography and etching processes. The objective of lithography is to translate a geometrical pattern to a given material layer. The basic steps of standard contact lithography are shown in Fig.1, where the layer to pattern is on the substrate. First, a thick layer of photoresistive polymer (photoresist) is deposited on top of the layer to be patterned. Next, the photoresist is exposed to light through a mask with opaque areas corresponding to the desired pattern. Due to such illumination, the solubility of the photoresist to developers becomes very different between shadowed and illuminated areas, Fig.1(a). The photoresist is then developed to obtain the desired pattern, which may be that of the mask (positive photoresist) or its complementary (negative photoresist), Fig.1(b). The pattern in the photoresist is then transferred to the target layer using selective etching techniques, Fig.1(c). Finally, the remaining photoresist is chemically stripped, Fig.1(d).

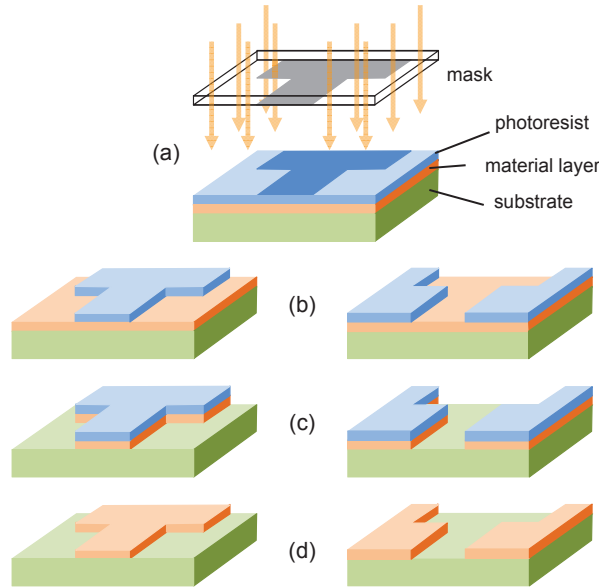


Fig. 1 Photolithography-etch process with either positive (left) or negative (right) photoresist: (a) exposure to light through the mask, (b) photoresist develop, (c) layer etch, (d) photoresist removal.

MEMS technology, on the other hand, has unique requirements and a growing set of applications that makes it clearly depart from IC fabrication [1, 2]. A clear first

difference is that MEMS may make use of thicker deposited or grown layers and deeper etchings. It may well be the case that even the whole substrate is to be etched in some parts of the wafer. Second, MEMS fabrication involves wider variety of materials, including quartz, ceramics, polymers, glass, piezoelectric and magnetic materials, etc. As a consequence, processes such as electroplating, wafer bonding, molding, anisotropic wet etching or deep reactive ion etching, are more common, or specific, of MEMS fabrication. Third, some devices must be processed on both sides of the wafer, thus adding front-backside alignment as a technological necessary requirement for certain devices. Fourth, MEMS devices include moveable mechanical parts such as beams and membranes that must be released. Additionally, the mechanical properties must be carefully controlled to avoid release distortion due to phenomena such as residual stress or stiction. Obviously controlling the mechanical properties of layers requires considerable effort. Putting all this together, a remarkable characteristic of MEMS technology is the existence of multiple and very diverse MEMS fabrication processes. This is specially true in the energy harvesting area, where many different processes are designed in order to obtain tailored mechanical properties of the devices. This fact represents in itself a large depart from what is the more common situation in IC technology.

2.2 Addition Processes for MEMS

Addition of materials onto a wafer is basic in MEMS. Process steps such as doping, thermal oxidation and epitaxy are inherited from IC technology. For instance, diffusion and ion implantation techniques are used in MEMS, but not in the same fashion as in IC technology. In the latter case, the objective is to have a very strict control on the electrical properties of the devices. In the MEMS case, though, the goal can be simply to convert a resistive layer into a quite good electrical conductor.

Thermal oxidation is a simple process used to grow good-quality thin films of silicon oxide on silicon substrates. The substrate is immersed into an oxygen-rich environment, which can be wet/liquid or dry/vapour. High temperatures from 800°C to 1100°C speed up the chemical oxidation of the substrate. However, as the thickness of the oxide layer increases, the substrate surface becomes harder to reach for the oxygen molecules. This effect causes non-linear reduction of growth rate for thicknesses greater than 100-200 nm.

Other addition, or deposition, processes come also from IC technology, but due to above mentioned expansion to new applications the variety of specific MEMS processes is growing continuously. The next sections will focus on the physical and chemical deposition processes mostly used for MEMS.

2.2.1 Physical Deposition

Physical deposition implies the direct transfer of a material from a certain source on the wafer surface. Examples are evaporation, sputtering and casting. Evaporation and sputtering are often used to deposit metals such as copper, gold and aluminium, among others. Evaporation is also used to deposit polymers. Casting is a common method to deposit polymers and glass. The thickness of deposited layers can range from a few hundreds of nano meters to microns. These processes are made at low temperatures, and may be therefore compatible with previous steps processes executed on the wafer. On the other hand, the quality of the layers (e.g. density of defects, resistivity, etc.) is not as good as when deposited by chemical methods.

- In **Evaporation** the source material and the wafer are placed inside a vacuum chamber. There, the source material is heated until it boils and evaporates. Being in vacuum, the evaporated molecules freely travel and condensate on all surfaces inside the chamber, including the wafer. A method to heat the source material consists on placing it in a tungsten chest and then applying high current. A high-energy electron beam or a laser targeting the source material are other common heating methods that serve to speed up the process.
- **Sputtering** is also performed inside a vacuum chamber. The chamber contains the source material, here called target, the destination wafer and gas plasma at low pressure. RF power is applied to generate gas ions and accelerate them towards the target. This causes extraction, or sputtering, of target atoms. Sputtered atoms travel and condensate on all surfaces inside the chamber. Sputtering is performed at lower temperature than evaporation.
- In **Casting** the source material is first dissolved in a liquid solvent. Then the solution is dropped on the wafer either by piping or spraying techniques. Next, the wafer is spun to spread the solution uniformly over the entire surface (spin coating). A material layer, with thickness that can range from the nano scale to tens of microns, is obtained once the solvent has evaporated. Due to their solubility in organic solvents, casting is common practice for the deposition of polymers, including photoresists used in photolithography.

2.2.2 Chemical Deposition

In this case, the source material is obtained from a chemical reaction taking place close to the wafer. Favourable conditions to excite and control the reaction, such as temperature, pressure, electric field or presence of plasma, are provided by specific equipment, which also provides means to remove the by-products of the reaction.

- **Chemical Vapour Deposition (CVD)** is done placing the wafer inside a reactor. A chemical reaction among two or more gas species produces the source material, which condenses on all surfaces inside the reactor, wafer included. CVD yields thin layers with almost-uniform thickness and good coverage, even on

stepped topographies. A variety of materials, including polysilicon, silicon nitride, silicon oxide, phospho-silicate glass (PSG), ceramics and plastics, can be deposited. Some materials are unpopular because of reactor contamination or due to the hazardous by-products they generate.

Low Pressure CVD (LPCVD) is performed at high temperature (from 500°C to 800°C). It yields fair material properties and layers with uniform thickness, but slow deposition rates. As an example, polysilicon deposition is achieved by decomposition of silane gas (SiH_4) into solid silicon and hydrogen gas under temperatures around 600°C. Plasma Enhanced CVD (PECVD) is performed at lower temperature because plasma adds extra energy to the gas mixture, but the layers have inferior quality than LPCVD ones. PECVD is often used for fast deposition of low-quality silicon oxide.

- **Electroplating** is a generic technique with many industrial applications. In MEMS, it is mainly used to deposit metals such as nickel and gold. The surfaces on which we want to deposit the corresponding metal are previously coated with a conductive material, if they are not conductive in themselves. Then the wafer is immersed into a liquid electrolyte solution. By applying a voltage between the wafer and an electrode also immersed in the solution, a reduction-oxidation reaction is excited. As result, wafer surfaces are coated with the source material. This way, nearly-uniform metal layers with thickness ranging from microns to tens of microns can be deposited.

Some appropriate chemical mixtures allow the reaction to take place without applying any external voltage, nor using contacts or electrodes within a liquid. In this case, known as electroless plating, the reaction is excited by the electrochemical potential between the solution and one or more materials on the wafer. However, the reaction behaves spontaneously and results such as deposition rate and layer thickness are difficult to control.

2.2.3 Wafer Bonding

The objective of wafer bonding is to obtain a permanent contact of two wafers. This process can be performed also at die level or at device level. Wafer bonding allows addition of materials obtained from different processes, but is also highly useful for other processing and post-processing purposes, such as planarization, wafer sealing in vacuum, packaging, or MEMS-IC integration.

Wafer bonding can be performed in many ways, chemical or physical, depending on materials to join and compatibility with other fabrication processes. In general, three subsequent steps are applied: 1) wafer pre-processing (cleaning and pre-treatment of the surfaces to contact; if needed, addition of intermediate layers), 2) wafer alignment and contact (it usually yields weak adhesion), 3) annealing and bond consolidation (by temperature, pressure, electric field, intermediate layer hardening, etc.).

Let us distinguish among direct and indirect bonding processes:

- **Direct bonding** is performed from wafer to wafer contact. The process is activated and enhanced by temperature or electric field. For example, silicon-to-silicon bonding is achieved with annealing temperatures around 800°C, a value often not compatible with other processes. Plasma enhanced bonding allows to decrease the temperature to 400°C or less. In anodic bonding, the wafers are stacked and placed between two electrodes, where voltage is applied. This low temperature process is mostly used for glass-to-silicon and glass-to-metal bonding. In thermocompression, pressure force and temperature are applied simultaneously to the stacked wafers until solid diffusion occurs. This process is used for metal-to-metal bonding.
- In **indirect bonding**, an intermediate material is placed between the wafers. This material provides long-time adhesion properties and reduces the relevance of the properties of the surfaces to contact (e.g. defects or topography). In adhesive bonding, polymers such as BCB (benzocyclobuten) or SU-8 (a negative photoresist) are used. Annealing is performed at relatively low temperature, with no voltage required. Since the wafers are not in direct contact, bonding of many different materials is enabled. In glass soldering, a glass layer with low melting point is used as intermediate material. In eutectic bonding, the intermediate material is a metal alloy. This alloy goes directly from solid to liquid state at temperatures far below the melting points of the metals involved. This way, good quality aluminium-to-silicon and gold-to-silicon bonding is achieved.

2.3 Etching Processes for MEMS

Etching processes are crucial in MEMS fabrication. Selectivity of etchant species against protection (masking) materials, substrates and the target material is a major issue, but etch rate, etch uniformity and temperature are also key characteristics. Let us first distinguish between wet and dry etching processes.

2.3.1 Wet Etching

Wet Etching is relatively simple and cheap. It allows to attack a material by immersing the wafer into a liquid etchant. The etchant chemically reacts with the material in unprotected areas. Wet etching can be isotropic or anisotropic.

- **Isotropic wet etching** is a classical technique performed to remove a wide range of materials, including semiconductors, dielectrics, metals or polymers. When used for patterning purposes, isotropic etch causes undercutting: the chemical reaction attacks the walls under the protection mask and produces a lateral etch effect, Fig. 2(a). The amount of undercutting is the same distance than etch depth, thus it affects pattern transfer precision.
- **Anisotropic wet etching**. Solubility properties of crystalline materials may vary with crystal orientation. In silicon, potassium hydroxide (KOH) and ethylene

diamine pyrocatechol (EDP) have different etch rates along the three crystallographic planes. For example, KOH yields etch rate selectivity of 300:1 or higher between the $\langle 100 \rangle$ and $\langle 111 \rangle$ planes. This means that etching can be virtually stopped on certain planes, and therefore substrates can be "sculpted" to produce a variety of structures. As an example, a trench is built in Fig. 2(b).

The alignment of the mask against the crystal planes, the etchant used and the process time are key factors. Additionally, precise temperature control and gas reflux systems are required to keep the etchant concentration constant during the process, and therefore the etch rate. Wet etchant and related by-products are hazardous substances that may cause handle and environmental safety problems. Anisotropic wet etching produces characteristic geometrical forms, since planes are not vertical to the surface when etching holes or trenches, as seen in Fig. 2(b). This implies large silicon consumption, loss of precision in pattern transfer and limits what structures are possible or not.

2.3.2 Dry Etching

In dry etching, the wafers are placed inside chambers that contain either gas or plasma reacting with the target material. In general, dry etching yields better etch performance than wet etching, but at noticeable higher costs due to the more sophisticated equipment used.

- **Isotropic gas etching** utilizes a gas with high etch selectivity against the mask protection material. As an example, xenon difluoride (XeF_2) has etch selectivity

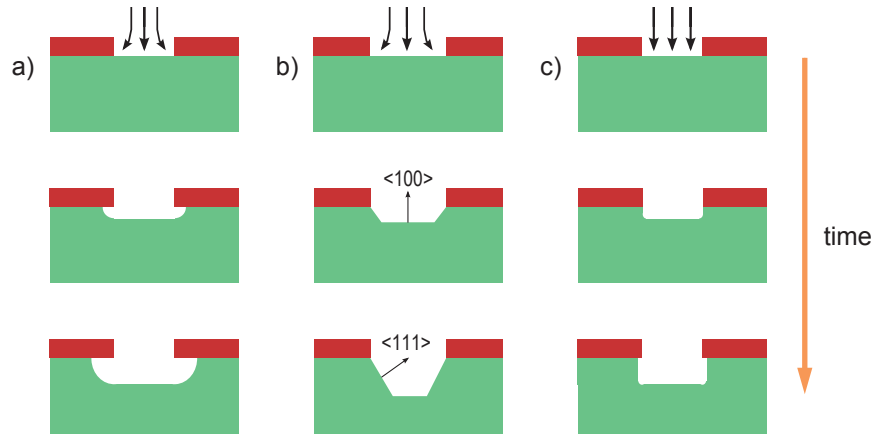


Fig. 2 Typical trench profiles obtained in silicon with different etch processes: (a) isotropic etching, (b) wet anisotropic etching -two crystallographic axes shown-, (c) anisotropic dry etching.

of silicon versus silicon oxide up to 10,000:1, whereas selectivity versus silicon nitride is around 100:1.

- **Plasma etching** is performed inside a specific reaction chamber that contains chemically active gas species at low pressure and applies an electric field to such gas. The electric field creates electrically charged gas radicals, which chemically react with wafer materials. In addition, the electric field may cause a physical etch effect: the charged radicals accelerate until they hit and sputter wafer materials. The physical etch component is anisotropic, whereas the chemical component is isotropic and material selective.
- **Reactive Ion etching (RIE)** is a special kind of plasma etching. In RIE, RF power is applied to increase the physical component of the etching, therefore it can be more anisotropic than traditional plasma etching. Moreover, the chemical-isotropic and physical-anisotropic mechanisms can be balanced to obtain etched features with rounded to nearly-vertical sidewalls. However, the process has many parameters to adjust and this implies long time-development until the desired balance is achieved. In practice, RIE is limited in etch depth (e.g. tens of microns for silicon) and etch rate (e.g. typical values around $1\mu/\text{min}$ for silicon). The next section focuses on Deep RIE, a special class of RIE that has gained enormous popularity in modern MEMS fabrication.

2.3.3 Deep Reactive Ion Etching

Deep Reactive Ion Etching (DRIE) is a highly anisotropic process aimed at creating deep holes and trenches in silicon, with high aspect ratios and nearly-vertical side walls. It was first developed by the German company Robert Bosch GmbH [3, 4]. The process is performed at room temperature. DRIE strongly improves etch performance against traditional anisotropic dry and wet etching techniques: silicon etch depths up to $750\mu\text{m}$ at rates up to $25\mu\text{m}/\text{min}$ are achieved typically. Etching uniformity at wafer scale is also improved.

A DRIE process performs RIE in small depth increments by alternating two different gas mixtures in the reactor:

1. The first mixture (e.g. SF_6 for silicon) provides standard RIE etch of the substrate, or another thick layer, through a window opened in a mask material (e.g. photoresist, silicon oxide, silicon nitride and metal, among others). This results in nearly vertical etching of the substrate.
2. The second mixture (e.g. C_4F_8) deposits a passivation layer. This layer dissolves very slowly in the chemical part of the subsequent RIE etch. The RIE directional ions attack the passivation layer at the bottom of the etched area. Then this bottom layer is sputtered off and the substrate becomes exposed to chemical etch.

An etch-passivation cycle lasts only for seconds. It is repeated many times, resulting in a large number of small etch steps taking place only at the bottom of quasi-vertical sidewalls, Fig.3. However, the sidewalls have slightly undulated shapes,

with typical amplitudes from tens to a few hundreds of nano meters. Cycle times can be adjusted to a trade-off between smoother walls and higher etch rates [5].

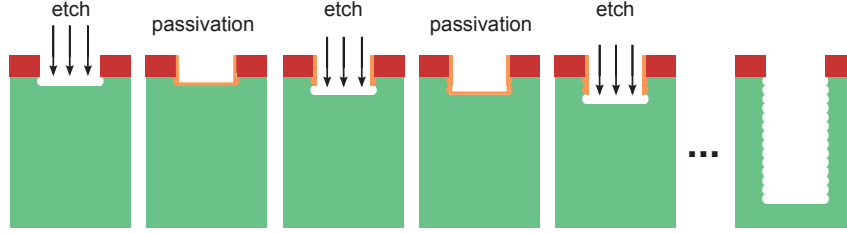


Fig. 3 Successive etch and passivation steps of a DRIE process.

Specific DRIE recipes have been developed for materials other than silicon, including glass, silica, quartz, InP and polymers. DRIE of glass substrates is performed applying high RF power, but this implies that mask materials must be carefully chosen. Chemically amplified photoresists and polysilicon are typically used as mask materials in DRIE of glass. Metal masks are used in DRIE of polymers, but this is expensive due to the additional deposition and lithography steps they require.

2.4 MEMS fabrication strategies

2.4.1 Surface Micromachining

MEMS surface micromachining aims at building moveable structures by deposition and patterning of different layers on top of the substrate. The moveable parts of the devices are made of what are called structural materials. These materials are deposited on top of what are called sacrificial layers, previously deposited or grown to hold the structural parts. The sacrificial layers will be removed later during the fabrication process. This removal of the sacrificial layers is known as the release process.

As an example, Figure 4 summarizes a series of steps performed to build up a cantilever structure. First, the sacrificial layer (i.e. silicon dioxide) is deposited and patterned through a photolithography-etch process, Fig. 4(a). The uncovered area will be used to attach (anchor) the device to the substrate. The structural layer (e.g. polysilicon) is then deposited on top of the wafer, Fig. 4(b). Next, the structural layer is patterned to define the device, Fig. 4(c). Finally, the sacrificial layer is etched. As shown in Fig. 4(d), this creates a void, equal to the thickness of the sacrificial layer, below the beam.

MEMS surface micromachining has evolved directly from IC fabrication, but some strong differences arise. For instance, in surface micromachining only up to 7-8 masks and minimum feature sizes around $0.5\text{-}1\mu\text{m}$ are typically used; this de-

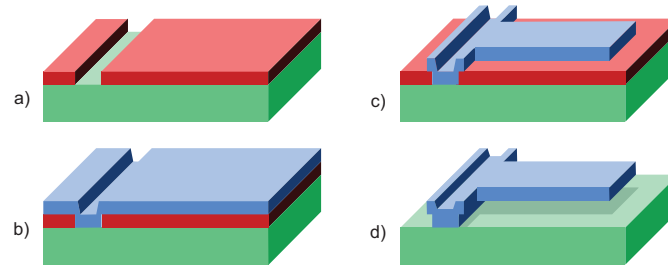


Fig. 4 MEMS cantilever fabrication using surface micromachining.

creases mask costs. However, in surface micromachining layers are thicker than thin films used in IC fabrication. This adds specific challenges to deposition and etch processes, including topography-related issues, since after 7-8 successive layer deposition and etch steps the vertical dimensions of structures can be any ranging from zero to tens of microns.

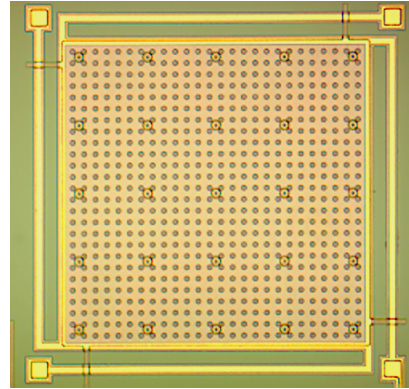
Another difference is that MEMS fabrication must take special care to control the mechanical properties, such as density, stress and Young's modulus, of structures to release. These properties are highly sensitive to the temperatures applied during fabrication. For example, successive heating and cooling can generate residual stress between two stacked layers due to the different thermal expansion coefficients of the materials. If one of such layers is removed, the released structure would not be flat and exhibit either tensile or compressive stress deformation, thus affecting the expected mechanical performance.

Finally, during the release process the surface tension of wet etchant can force contact between fixed and moveable parts of a device and cause stiction failure: the adhesion forces generated in the contact are strong enough to deform and permanently attract these parts. Using dry etching, critical point drying (CPD) during the final phase of wet etching, increasing the surface roughness or coating the layer with low surface energy materials are techniques used to prevent stiction. For devices with large areas to release, as the one shown in Fig. 5, it is common practice to etch regular grids of holes in the structural layer. This enables efficient diffusion of wet etchant during the etch of the sacrificial layer below.

Since surface micromachining is relatively close to IC fabrication, it constitutes the most frequent basis to develop monolithic microsystems, on which electronic (e.g. CMOS) and mechanical components are fabricated on the same substrate. The properties of the substrate are less important in surface micromachining than in other MEMS fabrication strategies, such as bulk or SOI micromachining. Then, surface micromachining enables the use of substrate materials other than silicon, as glass, quartz, plastics or organic polymers.

On the other hand, surface micromachining is not suitable to fabricate structures with large moveable parts, to use layers thicker than $2\text{-}5\mu\text{m}$, or to build features with the high aspect ratios that some MEMS applications demand. Additionally, some

Fig. 5 Top view of an electrostatic MEMS, taken from [6], fabricated with surface micro-machining. A $360 \times 360 \mu\text{m}^2$ polysilicon plate is held by four arms in "L" anchored to the substrate at the other ends. The plate is suspended over the substrate through a $2 \mu\text{m}$ air gap and a $0.65 \mu\text{m}$ silicon nitride layer.



geometrical structures are not possible to achieve, giving room to other fabrication strategies, such as bulk and SOI micromachining.

2.4.2 Bulk and SOI Micromachining

Unlike surface micromachining, bulk micromachining aims at the creation of MEMS structures within the substrate. It is based on selective deep etching of materials such as silicon or glass. Bulk micromachining fabrication processes that combine anisotropic and isotropic wet etching have been widely used to obtain a variety of mechanical structures in silicon.

Figure 6 illustrates the fabrication of a silicon cantilever. A mask material (e.g. silicon dioxide) is first deposited on top of a silicon wafer. Then it is patterned by a lithography-etch process, Fig. 6(a). A subsequent boron diffusion is performed in the uncovered substrate area. The p^+ doped area becomes resistant against wet etch species.

Once the initial mask removed, a second protection layer (e.g. polyimide photoresist) is deposited and patterned, see Fig. 6(b), where the dashed line encloses the boron diffusion. Next, anisotropic wet etching is applied to chemically attack the uncovered surface. Due to different etch selectivity along crystallographic planes and to the resistance of the p^+ area, the substrate trench and the suspended structure shown in Fig. 6(c) are obtained. The last step is the removal of the protection layer, Fig. 6(d).

Bulk micromachining techniques based on wet anisotropic etch of silicon are widely used in MEMS. However, these techniques have some issues. First, the cost in silicon is high, since large wafer areas are usually etched to obtain a unique device. Second, the process limits which geometrical structures can be done and which can not. Third, wet etching is unreliable to achieve structures with sizes below the micron scale.

In recent years, MEMS processes that use Silicon On Insulator (SOI) wafers in place of conventional silicon wafers have gained great popularity [1]. A SOI wafer

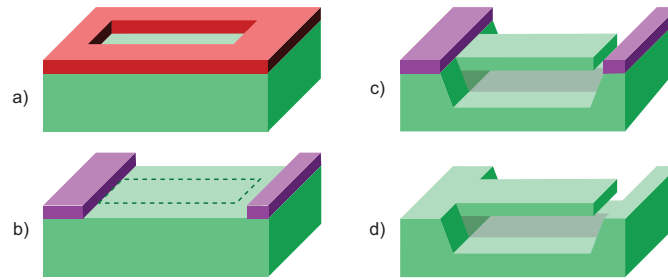


Fig. 6 MEMS cantilever fabrication in a silicon substrate using bulk micromachining.

is a stack of silicon, insulator and silicon layers. The MEMS structures are mainly fabricated in the top silicon layer, usually known as the device, or active, layer. This is good-quality crystalline silicon with well-known electrical and mechanical properties. In SOI wafers for MEMS the typical thickness of the device layer is tens of microns, well above the $1\mu\text{m}$ or less of SOI wafers used in IC fabrication. The buried insulating layer is typically silicon oxide, with thickness of microns or below. The bottom silicon layer, with typical thickness of hundreds of microns, is known as the handle substrate.

SOI-based MEMS processes allow to combine both bulk and surface micromachining techniques to obtain a rich set of structures. For example, the buried insulator can provide built-in stop for dry and wet etching processes performed in the device layer, but it can also be used to stop deep etch processes performed in the handle substrate. This way, features such as through-wafer holes, front or backside cavities of controlled depth, structure release from both sides of the wafers, full-wafer thickness suspended structures, etc. can be easily achieved. Surface micromachining techniques can be also used, mostly on the device layer. A commercial SOI-based MEMS process is described in section 2.4.4.

2.4.3 Multi-Project Wafer Processes

Some MEMS foundries offer multi-project wafer (MPW) processes. These are robust and closed fabrication processes that provide well-known and reliable results. Additionally, MPW processes can be inexpensive, since wafers can be shared among several users. Their use facilitates users to focus on the device design, avoiding challenges associated with process development. MPW processes offer CAD tools such as device templates, design rules for layout checking and electrical and mechanical parameters for simulation. In general, MPW processes have not been targeted for commercial production, but used for research and prototyping. In recent years, some foundries have started providing specialized MPW services for low-volume production customers trying to reduce their design cost and time to market.

The first MPW process offered was a surface micromachining process developed by Howe and Muller [7, 8], with three polysilicon structural layers. Today, a number of MPW processes that use surface, bulk and SOI micromachining, electroplating and CMOS integration at wafer level are available. Some examples follow:

- MEMSCAP's MUMPS (Multi-User MEMS Processes) [9] offers PolyMUMPS, SOIMUMPS, MetalMUMPS and PiezoMUMPS. PolyMUMPS includes surface micromachining with three polysilicon structural layers and two silicon oxide sacrificial layers. SOIMUMPS combines SOI bulk and surface silicon micromachining. MetalMUMPS combines electroplating, surface and bulk micromachining, with nickel and polysilicon as structural materials. Finally, PolyMUMPS adds a piezoelectric layer to a process similar to SOIMUMPS.
- Sandía SUMMiT (Sandia Ultra-planar, Multi-level MEMS Technology) V [10] is a surface micromachining process similar to PolyMUMPS, but with five structural layers and including planarization.
- InvenSense's NF Shuttle process [11] offers MEMS-CMOS integration. MEMS SOI devices and CMOS circuitry are fabricated on separated wafers. Then the wafers are bonded together using low-temperature eutectic bonding.
- Teledyne-DALSA's High Voltage CMOS/DMOS Technology with MEMS Post-Processing [12]. This process combines high voltage CMOS circuitry and simple MEMS structures, with metal as structural material.
- Lionix's TriPleX MPW and Fluidic MPW processes [13] are specifically targeted to devices for either integrated optics or microfluidic applications.

2.4.4 The PiezoMUMPS process

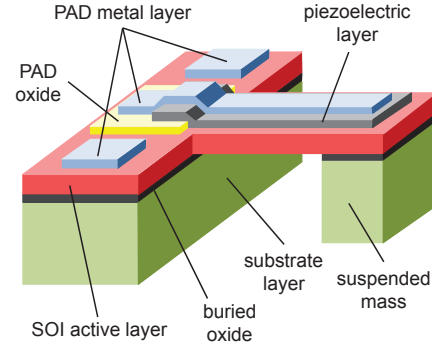
The PiezoMUMPS process [14] was introduced by MEMSCAP in 2013 as a response to the growing interest in piezoelectric MEMS. This low cost and low temperature process evolved from the previous SOIMUMPS. It uses the same SOI wafers and inherits some well-known bulk and surface micromachining features. The SOI wafer is a stack of, from bottom to top, a silicon substrate layer ($400 \pm 5 \mu\text{m}$), a buried silicon oxide layer ($1 \pm 0.05 \mu\text{m}$) and the SOI device layer ($10 \pm 1 \mu\text{m}$). A thin oxide layer is present on the bottom surface.

The process includes deposition and patterning of an Aluminium Nitride (AlN) piezoelectric film on top of the SOI device layer. It also includes deposition and patterning of additional metal and silicon oxide layers. Five mask levels are used. The minimum feature size for the SOI layer is $2 \mu\text{m}$, making structures with aspect ratios up to 5:1 possible.

In order to illustrate the process flow, let us apply it to obtain the unimorph piezoelectric cantilever shown in Fig. 7, a structure rather similar to resonators used in energy harvesting applications [REFS].

The process starts with LPCVD deposition of PSG on top of the SOI layer, Fig. 8(a), followed by thermal annealing in argon atmosphere, 1050°C for 1h. Due to the corresponding phosphorous diffusion, the surface of the SOI device layer

Fig. 7 Unimorph piezoelectric cantilever structure with a full-wafer thickness mass suspended at the free end. The two outer metal PADs provide electrical contacts to the SOI active layer, while the one in the middle contacts the piezoelectric film.



becomes highly conductive ($15\text{-}25\Omega/\text{sq}$). After that, the PSG layer is completely removed by wet etching. Next, a $0.2\mu\text{m}$ layer of thermal oxide is grown on top surface. Through a photolithography-etch process using positive photoresist and RIE, the oxide is patterned accordingly to the PADOXIDE mask, Fig. 8(b).

The first material deposited is a $0.5\mu\text{m}$ thick AlN piezoelectric layer. A reactive sputtering process is used for this purpose. Then, using photolithography with positive photoresist and wet etching, the PZFILM mask pattern is transferred to the AlN layer. That is followed by photoresist strip, Fig. 8(c).

Next, a metal stack composed of 20nm of Chrome and $1\mu\text{m}$ of Aluminium is deposited and patterned using the following lift-off process: the wafer is coated with negative photoresist and exposed to light through the PADMETAL mask, then the photoresist is developed and the metal layer is deposited over the entire surface by evaporation; finally, the photoresist is dissolved to leave behind metal only in the uncovered (developed) areas, Fig. 8(d). This process allows to define $3\mu\text{m}$ minimum metal features and spaces with $3\mu\text{m}$ of alignment tolerance.

The $10\mu\text{m}$ SOI device layer is patterned using positive photoresist and the SOI mask. The pattern is transferred to silicon using a specific DRIE process, based on Inductively Coupled Plasma (ICP) technology, that prevents undercutting of the silicon when the etch reaches the buried oxide layer. After etching, the photoresist is stripped, Fig. 8(e). Since the surface of the device layer is heavily doped, the separated metal features deposited on this layer will be electrically contacted unless they are also separated by a trench feature defined by the SOI mask.

Next, a thick polyimide coating is applied onto the front surface of the wafer, Fig. 8(f). This coating holds the wafer together through the next process steps. The wafer is then reversed and negative photoresist is deposited on the bottom surface. Next, the photoresist is patterned accordingly to the TRENCH mask. A RIE process is then used to remove the bottom oxide in the uncovered areas. Subsequent DRIE is performed to etch the TRENCH mask patterns through the substrate, until the buried oxide is reached. When etch completed, the remaining photoresist is stripped. Finally, wet etching is used to remove the oxide layer in the uncovered areas. As result, the substrate layer is patterned accordingly to the TRENCH mask, Fig. 8(g).

Finally, the front side protection coating is removed using a dry etch process. This releases the mechanical structures in the SOI active layer located over through-substrate holes, Fig. 8(h). Figure 9 shows two photographs of a low-frequency MEMS resonator fabricated with PiezoMUMPS technology.

3 Nonlinear mechanisms used in energy harvesting with MEMS

The first approach made to EH has been based on the use of linear resonators. The main disadvantage of linear devices is that they present a small bandwidth and therefore are able to retrieve energy from only a part of the spectrum of the mechanical excitations. To solve this issue, the use of resonators exploiting nonlinear mechanisms has been proposed as a way to, in some cases, dramatically enhance the

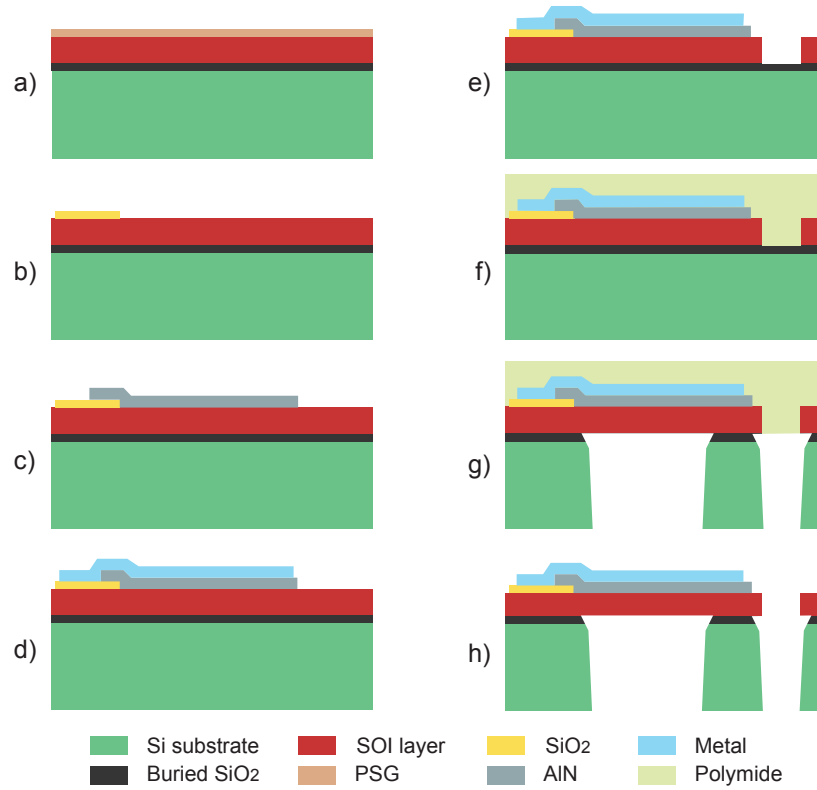
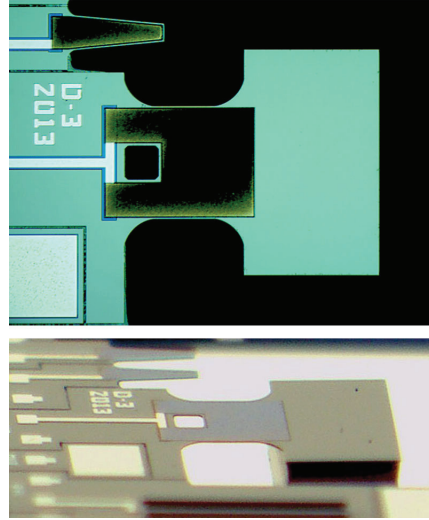


Fig. 8 Piezo-MUMPS fabrication process steps: (a) silicon doping, (b) thermal oxide deposition and patterning (PADOXIDE), (c) piezoelectric layer deposition and patterning (PZFILM), (d) metal layer lift-off (PADMETAL), (e) silicon device layer patterning (SOI), (f) polyimide coating, (g) substrate layer patterning (TRENCH), (h) structure release.

Fig. 9 Top and lateral view of a piezoelectric MEMS resonator fabricated in the PiezoMUMPS batch reported in [15]. Cantilever dimensions are $1100\mu\text{m}$ long and $500\mu\text{m}$ wide. The mass suspended at the free end has an area of $600\mu\text{m} \times 1000\mu\text{m}$ and full-wafer thickness ($410\mu\text{m}$). The first mechanical resonance mode is at 1.22kHz .



performance of these devices. In this section we will introduce the main design techniques used in MEMS devices to implement nonlinear mechanisms such as bistable potentials, nonlinear springs and impact energy transfer.

3.1 Bistable potentials

3.1.1 Bistable potentials obtained with permanent magnets

One of the methods used in the literature to produce bistable potentials consists on suitably placing a permanent magnet on top of a cantilever and another one fixed to the structure frame. By placing both magnets so that in the rest position they face with the same polarity a bistable potential is easily generated. In [16] a MEMS is presented on which the bistable potential is achieved by placing the permanent magnet at the tip of a BESOI (bulk etched SOI) cantilever, and this in front of another permanent magnet such that the polarity of both magnets is opposed at the nearest point, see Figure 10. This configuration of magnets provides a repulsive force such that the rest position of the cantilever is no longer stable.

Regarding the fabrication the authors use a BESOI technology with a bulk $450\mu\text{m}$ thick, $2\mu\text{m}$ of buried oxide, a $15\mu\text{m}$ crystalline silicon active layer and several deposited layers with oxide, polysilicon and metal. The cantilevers are $2000\mu\text{m}$ long with different widths in the range below $800\mu\text{m}$. The permanent magnet deposited at the tip of the cantilever has a cylindrical shape and is made of NdFeB. The whole structure is usually manually assembled or microassembled, [17], since the fabrication process of the magnets is not compatible with the MEMS fabrication.

This difficult placement results either in non-repeatability or high production cost.

The obtained bistable potential is assumed to be that of a nonlinear pendulum governed by a double well nonlinearity:

$$U(x) = kx^2 + (ax^2 + b\Delta^2)^{-3/2} + c\Delta^2 \quad (1)$$

where Δ is the distance between the south poles of both, see Figure 10, and parameters a, b and c depend on the specific geometry of the cantilever and its mechanical properties. Taking into account this kind of potential, the equation governing the dynamics of the inverted pendulum with the bistable potential is [18]:

$$m\ddot{x} = \frac{dU(x)}{dx} - \gamma\dot{x} - K_v V(t) + \sigma\xi(t) \quad (2)$$

where the $\gamma\dot{x}$ term represents mechanical damping, the $-K_v V(t)$ represents the energy transfer to the electrical domain and $\sigma\xi(t)$ corresponds to the external vibration force driving the pendulum.

The main disadvantage cited against this type of structures is the presence of moving magnets, since they can generate fluctuations in the magnetic field which can affect other parts of the circuit, [19]. Furthermore, another disadvantage is the placement itself of the permanent magnets on the MEMS structures, which is usually made microassembled by hand. Electroplating [20], though, has been proposed as an alternative means to produce MEMS compatible permanent magnets, not manually assembled, [21, 22].

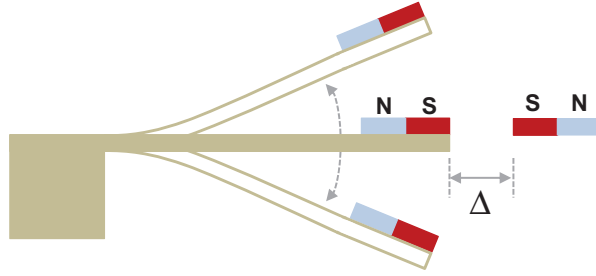


Fig. 10 Schematics of the structure proposed in [16]: a cantilever with a fixed magnet at the tip, facing another magnet with south pole polarities facing each other. The rest position of the cantilever is no longer stable and whole structure is bistable.

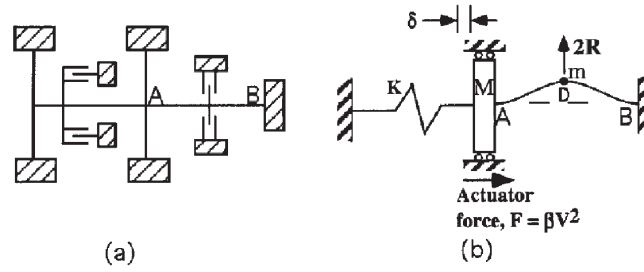


Fig. 11 Schematics of the structure proposed in [24]: a) principle of actuation for a tunable bistable mechanism; b) model of the structure.

3.1.2 Bistable potentials obtained by buckling or snap-through instability

Buckling has been used in energy harvesters to obtain a bistable potential. As it has been very well explained in [23], by simply holding a business card between fingers and bowing it, a bistable system is created. A force normal to the surface of the card can make it snap from one stable position to the other. In order to obtain this kind of behaviour in MEMS structures, the axial load necessary for this buckling behaviour may come from residual stress of the fabrication process, or from the actuation with comb drives conveniently placed in the device to transmit an axial load to the corresponding beam [24]. Other mechanisms have also been established to create bistable mechanical structures such as: clamp mechanism with actuator to switch between stable states [25], or two curved parallel beams clamped in the center [23] not relying on residual stress to obtain the buckling behaviour.

In [24] a tunable bistable mechanism is presented where an actuator generates a tunable axial compressive force on a beam, which is also subjected to a transversal force (see Figure 11). The actuator is used to establish the necessary compressive force on the buckling beam to obtain the bistable potential. The beam is located between points A and B in the schematics of Figure 11.a). The actuator force, proportional to the square of the voltage applied on the comb drive (Figure 11.b), is shared between its own springs (located to the left in Figure 11.a)) and the buckling beam. The force transverse to the beam is generated by two comb drives vertically arranged between points A and B in Figure 11.a). A photograph of the device can be observed in Figure 12. The main actuator spans an area of $1 \times 1 \text{ mm}^2$, has 800 comb drives and is supported by 6 beams, held by anchors. It has been designed to generate only compressive stress on the buckling beam. The fact that this compressive force is exerted by the comb drives of the main actuator is what makes this device tunable, since the bistable potential can be modified as a function of the voltage applied to the main actuator.

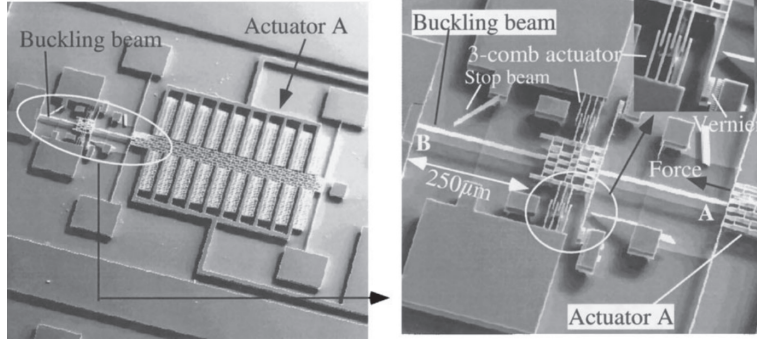


Fig. 12 Left: overall photograph of the actuator and the bistable buckling beam of [24]. Right: detail of the beam and up and bottom comb drives.

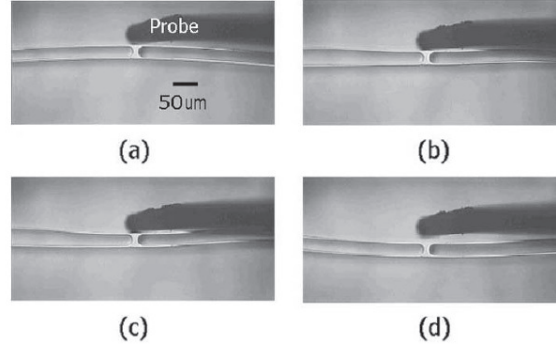


Fig. 13 Bistable mechanism of double curved beams, [23], a) initial stable position, b) applied force deflects the double beams, c) more force generates more deflection, d) beams at the second stable position.

In [23] the authors present another bistable device that does not rely on pre-stress of the beam to produce buckling. They use two curved centrally-clamped parallel beams to generate the bistable potential, see Figure 13. A similar approach is taken in [26] on which pre shaped buckled beams are designed [27]. In general the physics of curved arches requires additional analysis in order to predict the nonlinear effects due to the curvature of the structures and the snap-through instability [28, 29].

In [19] a bistable potential is obtained by a different structure on which a central mass is connected with two slightly slanted rigid fixed links through flexural pivots. In this way two symmetrical stable positions can be achieved and therefore the structure presents a bistable potential. The equivalent mechanical model for the potential energy can be observed in Figure 14. The slant angle, namely θ_0 plays an important role in the definition of the elastic potential of the structure, since it

Fig. 14 Pseudo-Rigid Body Model of the first microstructure proposed in [19].

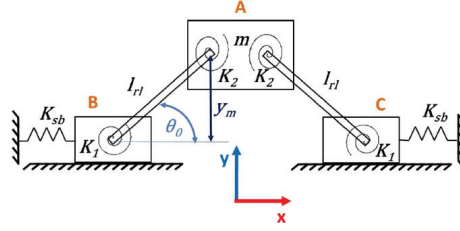
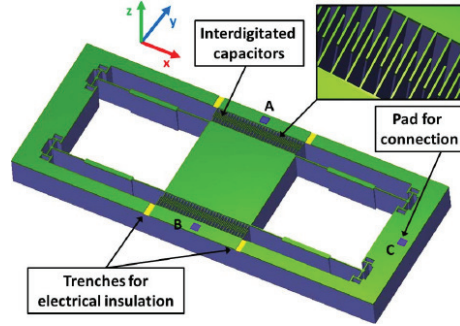


Fig. 15 Model of the final structure proposed in [19]. Pads 'A', 'B' and 'C' are for the electrical connection of the comb capacitors.



is used to generate the bistable potential (for θ_0 the potential is monostable), while at the same time it will generate an asymmetry in the elastic potential. The reason for this is that the slant angle makes easier to snap through from one of the states than from the other. The potential energy of the mechanical structure is difficult to analyze and the authors use FEM simulations to obtain the elastic potential. In the final proposed structure though, double fixed links are connected in a H configuration with a central mass. The whole thickness of the BESOI wafer ($467\mu\text{m}$) is used in the implementation of the arms. This is done in order to improve the mechanical stability of the design, specifically avoiding the appearance of unwanted vibration modes. The slant angle finally chosen is 0.5° . The sensing electrodes, consisting of a comb drive, are placed perpendicular to the direction of the fixed links and serve to extract the mechanical energy harvested by the mechanical structure, see Figure 15.

3.2 Nonlinear springs

The use of nonlinear springs has also been proposed to increase the effective bandwidth in energy harvesters. Nonlinearity in the spring stress-strain relationship can generate either a hardening, [30, 31], or a softening behavior, [32, 33]. In the first case the resonant frequency increases when the oscillation amplitude increases,

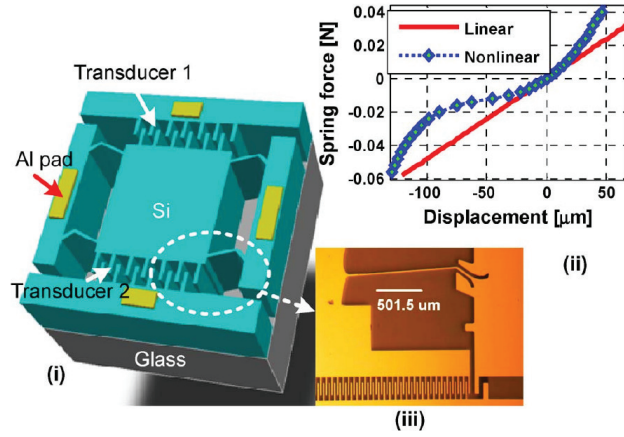


Fig. 16 i) Geometry of the device using nonlinear springs proposed in [33], ii) spring force as a function of displacement of the nonlinear spring calculated by FEM, iii) photograph of one the nonlinear springs in the device.

whereas in the second case the resonant frequency decreases with increasing oscillation amplitude. In general both phenomena can occur in a type of device, but depending on some condition (applied voltage, dimensions of the structure, etc) one of them dominates above the other, [34]. Nonlinearity in springs appears for large deflections. For example, in the case of thin fixed-fixed beams, or tethers, it appears when the displacement of the proof mass is comparable or larger than the thickness of the springs, resulting in an increase of the strain energy due to stretching of the neutral surface, [34, 35, 36]. This is obviously an unwanted phenomenon in linear devices whereas it is a desired feature in those applications, such as energy harvesting, on which nonlinearity is sought as a means to increase bandwidth.

The authors in [32] present a wafer thick resonator that has nonlinear springs for enhancing energy harvesting. The fabrication process consists mainly of a full-wafer-thickness dry etch that serves to delimit the inertial mass and the supporting nonlinear springs. This wafer will be anodically bonded to a Pyrex glass wafer that has been previously wet etched so that the inertial mass is free to move. Special care has been taken by placing dummy protective structures close to springs and capacitor fingers, to limit inward sloping sidewalls in places where the etch opening is of the order of the etch depth or larger. In this design the spring restoring force is approximated by a seventh order polynomial. Figure 16 shows a model of the proposed structure, a photograph of the nonlinear spring and also the relation between the force vs displacement in the nonlinear spring obtained by FEM simulations. As it can be observed in Figure 16.ii) the softening behavior is obtained only in one direction (negative displacement).

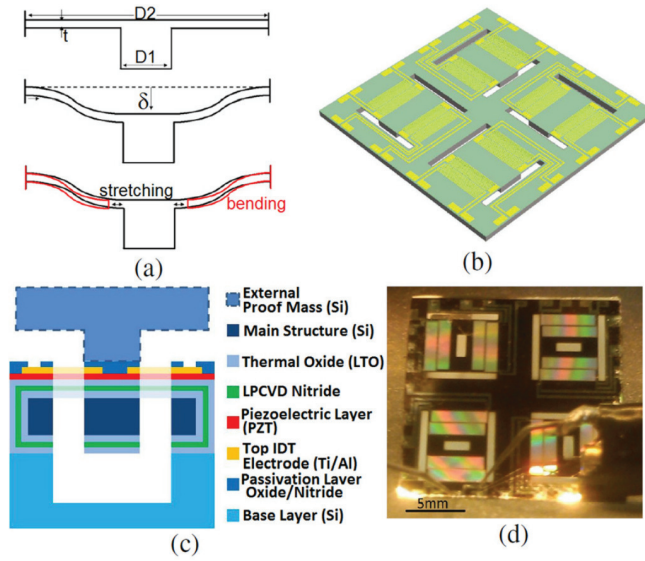
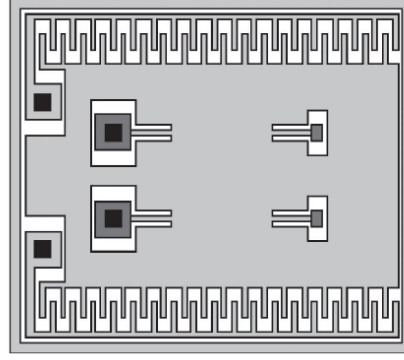


Fig. 17 Device proposed in [37]: a) displacement of the proof mass generates nonlinear bending and stretching strain in the supporting beams, b) general overview of the device with four beams supporting the main structure of the bulk silicon wafer. An external mass will be attached to the upper surface of the beams afterwards, c) cross section of the structure, d) photograph of the final device

The authors in [37] propose to use a clamped-clamped configuration for the supporting thin beams of a proof mass. Each beam is clamped between the proof mass and the supporting structure. This way, the displacement of the proof mass generates stretching. The only existence of bending would require lateral motion and, since the proof mass is in the center of a clamped-clamped beam, this is not possible. This effect is illustrated in Figure 17.a). The fabrication process includes several steps comprising both surface and bulk micromachining. The structural layer of the beams is composed of LPCVD silicon nitride and low temperature silicon oxide. The active layer consists of Ti/Al interdigitated electrodes, a PZT thin film and a layer of ZrO_2 . A PECVD passivation layer is finally added to protect the active layer and compensate the residual stress. After the structure has been fabricated external masses are attached to the upper surface of the beams to achieve a higher nonlinearity of the structure.

The authors in [38] propose an electrostatic harvester using a large mass subjected by nonlinear springs to increase the effective bandwidth. A schematic of the device can be seen in Figure 18 on which two comb drives are at the top and bottom, while the inertial mass is anchored in four points (dark grey areas in the middle of the inertial mass). The device has been fabricated with a commercial SOI process from Tronics Inc. The nonlinear regime is obtained at large displacements of the in-

Fig. 18 Schematic of the device proposed in [38]. Dark grey rectangles are mass-spring anchorages and black squares represent electrical pads. The displacement of the proof mass is in plane between comb drives.



ertial mass. The authors have fitted with a 7th order polynomial the nonlinear terms of the spring.

3.3 Nonlinear energy transfer by impact

The first proposed use of impact in energy harvesting application can be traced back to [39]. Impact actuation can be seen as an example of pulsed actuations, i.e., an actuation on which the velocity of the device is almost instantly changed. This type of excitation has been used to obtain self-sustained oscillations in MEMS resonators, [40, 41, 42].

An example of energy transfer by impact applied to EH can be found in [43, 44] where the authors propose the use of two cantilevers, one with a low resonant frequency (LRF) and another with a higher resonant frequency (HRF) that may impact each other. The structure of the proposed device can be observed in Figure 19. The LRF cantilever has a silicon inertial mass and has to be stopped by the HRF cantilever. To this purpose, a specific packaging has been designed. The LRF cantilever constitutes the excitation of the second one, the HRF cantilever. This results in a FUC, Frequency Up Conversion, on which the energy is transferred from the LRF cantilever to the HRF.

The simplified equations of motion are:

$$\begin{aligned} (m_0 + m_1)\ddot{z} + (c_0 + c_1)\dot{z} + (k_0 + k_1)z - k_1x_0 &= -(m_0 + m_1)\ddot{y}, & (z \geq x_0) \\ m_0\ddot{z} + c_0\dot{z} + k_0z &= -m_0\ddot{y}, & (z < x_0) \end{aligned} \quad (3)$$

The excitation cantilever, LRF, has as a proof mass m_0 , a damping coefficient c_0 and a spring constant k_0 . At a distance x_0 is placed the second cantilever with a mass

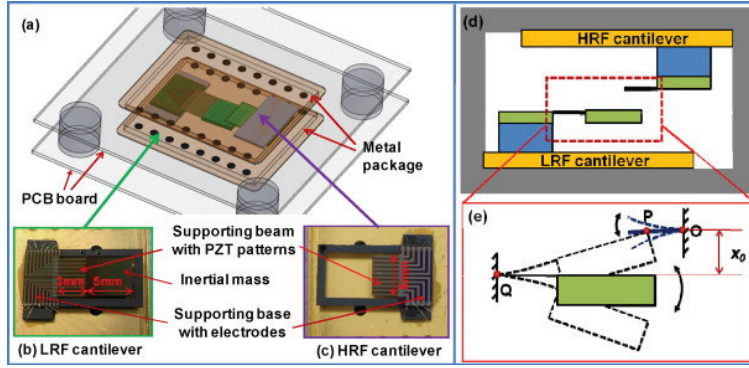


Fig. 19 Device proposed in [43]: a) Schematic of the overall system, b) LRF cantilever, c) HRF cantilever, d) schematic of the arrangement of both cantilevers inside the packaging, e) illustration of the impact between cantilevers.

m_1 , a damping coefficient c_1 and a spring constant k_1 . Both cantilevers interact when the displacement of the first one is greater than the distance between both resonators, $z \geq x_0$.

The fabrication process of the piezoelectric cantilever, [45], is started from a SOI wafer with a $5\mu\text{m}$ thick silicon active layer, a buried oxide of $1\mu\text{m}$ and the bulk of the wafer, $400\mu\text{m}$. On top of the active Si layer, multiple layer depositions are made (first one of Pt/Ti for the bottom electrode, second one of $3\mu\text{m}$ of (100)-oriented PZT, and third another metal deposition composed of Ti/Pt/Ti for the configuration of the top electrode). The metal depositions are made with sputtering and the PZT is deposited with a sol-gel process. The etching of the multi-layer is made with Ar-ion beam for the metals and the PZT layer is wet etched. The whole structure is passivated with a SiO_2 layer deposited by sputtering. Holes are made on the oxide layer to place contacts. The bulk of the SOI wafer is later etched from the backside to release the moveable parts while preserving the inertial mass.

For this application special care must be taken with the packaging because it must provide the correct separation between the cantilevers while at the same time one of them is placed upside-down (see Figure 19).

4 Transduction principles

The objective of this section is to present the specific requirements of electrostatic and electromagnetic transduction when used in energy harvesters. In particular the electrostatic transduction in some devices requires the presence of electrets. Electrets are dielectric materials on which permanent charge has been introduced. The movement of the electrets due to external vibrations can trigger currents in some

parts of the device from which energy can be retrieved. Piezoelectric transduction will be treated later in a separate section.

4.1 Electrostatic transduction

In electrostatic harvesters, the vibration energy is recovered by means of electrostatic force, which acts as a damping mechanical force. This kind of devices requires an initially pre-charged surface, so that the movement of a seismic mass generates a current flow in some part of a circuit. In order to provide this initial charge several alternatives have been proposed such as insulated floating electrodes, [46], electrets [47, 48] and also electret-less circuits that require an external starting voltage or current, [49]. Electrets have been extensively used although they may require unconventional steps in the fabrication process.

On the other hand, some papers in the literature present electrostatic energy harvesters avoiding the presence of electrets or even external circuits necessary for pre-charging the structure. This kind of papers focus on the exploited mechanical nonlinearity or other features and use standard power sources to harvest. In this subsection we will focus on electrets and we will present some examples of energy harvesters that make use of them.

Electrets are dielectrics on which a quasi-permanent charge has been injected, [50]. The lifetime of these charges can be very large. As an example, experiments on which a charge density has remained unchanged for 35 years are reported in [51]. Electrets present this charge, and therefore a stable built-in voltage, due to some previous ion injection, poling or application of a voltage. Among the materials most commonly used for electrets we find inorganic layers made of SiO_2 , a combination of SiO_2 and Si_3N_4 layers, [52], and also organic compounds based on polymers. Among the polymers compatible with MEMS processes we may find the amorphous perfluorinated polymer CYTOP (Asahi Glass Col., Ltd), [53, 54, 55, 56]. This polymer can provide up to four times more charge density than Teflon.

Among the methods used for poling electrets we may find: corona charging, ion implantation, contact charging, thermal poling, UV irradiation, soft X-ray irradiation and electron-beam irradiation. Charges have also been successfully injected into electrets with very inexpensive equipment such as ionic hair-dryers, [56]. Corona charging generates principally surface charge whereas electron beam and thermal poling produce volume, surface charges and polarization. Thermal annealing may follow the corona charging to increase charge stability by driving charges to the bulk of the material. Long term. Both SiO_2 and CYTOP present good charge stability, [55], an essential property.

The more conventional approach for using electrets includes planar electrets, [57], although they can also be deposited on vertical walls, [56, 58]. Vertical electrets are more difficult to produce since for example the corona method or ion implantation cannot be used. On the other hand vertical electrets are compatible with standard electrostatic comb drive actuation.

Fig. 20 Cross-section of the device proposed in [57]. The motion of the proof mass is indicated by the arrow. The proof mass is conductive.

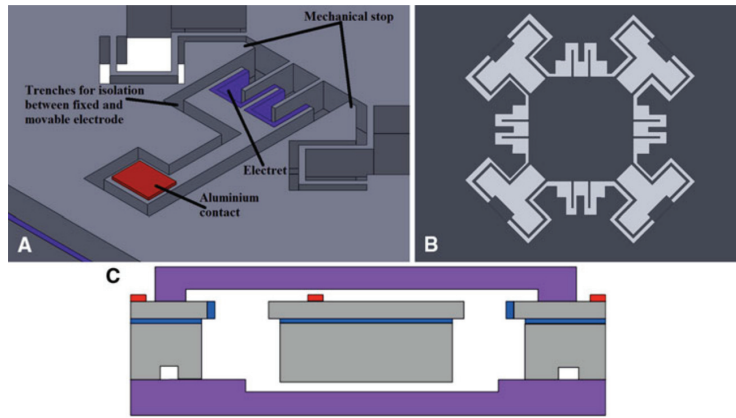
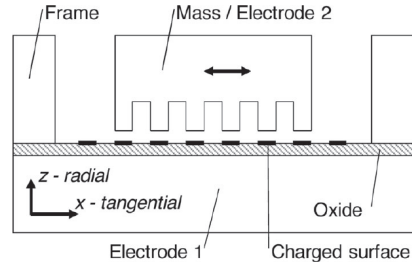
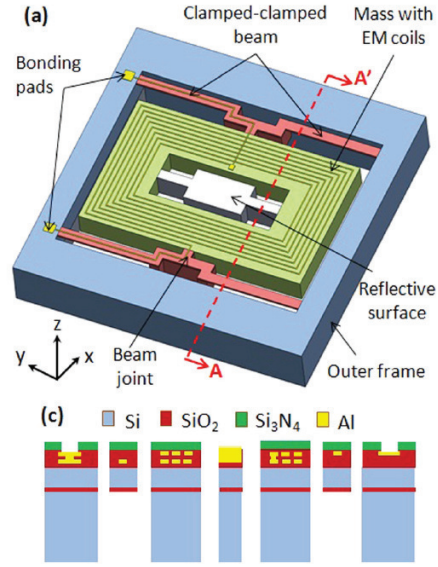


Fig. 21 a) Detail of the device proposed in [56], b) schematic of the overall device, c) cross section of the device (suspending beams not shown).

Examples of recent energy harvesters using electrets can be found in [57, 56, 59]. The authors in [57] propose an electrostatic energy harvester using an electret inside the active gap. Figure 20 shows a schematic of the device. The electret has been patterned in stripes on the bottom wafer whereas the proof mass, which is conductive, moves inside the potential generated by the electret. If a load is connected between electrodes 1 and 2, a current will flow and power will be transferred. Since the displacement of the mass can surpass a single electret stripe, frequency up-conversion may occur. This is because a single period in the proof mass movement can generate several electret stripe crossings and therefore several periods in the generated current.

The authors in [56] propose a 3D electrostatic energy harvester using sidewall electrets. The device allows to retrieve vibration energy in any direction due to the specific design that fixes an angle of 45° between the suspending beams and the

Fig. 22 Schematic of the electromagnetic harvester presented in [60]. A cross-section of the device is shown at the bottom of the figure. The thickness of the silicon active layer, used for the clamped-clamped beams is $5\mu\text{m}$ and the thickness of the bulk of the wafer is $400\mu\text{m}$.



comb drive electrodes with electrets, see Figure 21. The pull-in contact between electrodes is avoided by the presence of the mechanical stoppers shown in Figure 21.a). The electrets have been vertically placed on the surface of the fixed electrode fingers and are made of SiO₂. The authors have charged the electrets using an hair-dryer that is commercially called 'ionic hair-dryer' since it generates ions to compensate for the charge generated in hairs by combing. Electret charging with this method strongly depends on the exposition angle. Nevertheless, the authors are able to charge these vertically placed electrets by exposing them to the air flow for more time.

4.2 Electromagnetic transduction

In this kind of transduction, the energy is recovered in some coils present in the device as a function of the variation of a magnetic field. The variation of the magnetic field will be due to some vibration mode activated in the structure by the external acceleration from which energy must be recovered.

The authors in [60] propose a device for electromagnetic energy harvesting. This device uses a SOI wafer for which the thickness of the active layer and the bulk of the wafer are $5\mu\text{m}$ and $400\mu\text{m}$ respectively. The design has two thin clamped-clamped beams connected to a large mass by beam joints, see Figure 22. A cross section of the device can be observed in the same figure. The device presents a

two-fold objective to increase performance of the device: nonlinear force-deflection characteristic, an amplitude-stiffened Duffing-spring, and multi-frequency harvesting mechanisms by using different resonant modes of the structure (out-of plane 70.7Hz, torsion 85.78Hz and twist modes 147.92Hz). The electromagnetic harvesting is accomplished by placing a cylindrical magnet on top of the device that generates a magnetic field perpendicular to the surface of the device. The large mass integrates the EM coils that will be used to retrieve the electromagnetic energy. All three modes can generate large beam deflection and stretching strain, generating therefore a nonlinear response of the device.

The expression showing the equivalent force applied in the center of the clamped-clamped beam of the device is:

$$F = \left(\frac{\pi^4}{6} \right) \left[\frac{Ewh^3}{l^3} \right] x + \left(\frac{\pi^4}{8} \right) \left[\frac{Ewh}{l^3} \right] x^3 \quad (4)$$

where E is the Young's modulus, w , h and l are the width, thickness and length of the beam. The first term is due to the bending strain and produces a linear spring constant, whereas the second term, related to the stretching strain, produces the cubic term. Observing this expression the nonlinear term will be significant for displacements larger than the thickness of the beam [60].

5 MEMS devices based on piezoelectric transduction mechanism

This section describes the structures, materials and main properties of MEMS based on piezoelectric transduction mechanism. The piezoelectric properties of materials and a description of most common piezoelectric materials are included. Subsequently, cantilever beam structure with a tip mass is described due to its wide use in MEMS energy harvesters. The unimorph and bimorph cantilever structures are presented and discussed. Bimorph piezoelectric cantilevers allows higher output power while unimorph piezoelectric cantilevers are more manufacturable. Furthermore, it also reviewed the top-bottom electrodes, TPE, and interdigitated, IDE, electrodes configurations for unimorph cantilevers. These electrode configurations are used when 31 or 33 modes of piezoelectric materials are required. Finally, an application example of MEMS-based bimorph energy harvester is illustrated.

Piezoelectric transduction is an advantageous mechanism to convert vibration-to-electric energy for small scales as stated by Marin et al. [61] and Cook et al. [62]. Marin studied the relationship between the effective material volume (v) and the output power for different mechanisms. The output power for the piezoelectric mechanism is proportional to $v^{3/4}$, while that for the electromagnetic mechanism is proportional to v^2 . At volumes smaller than 0.5 cm^3 the electromagnetic transformation factor is reduced abruptly [61]. The piezoelectric mechanism has the highest energy conversion efficiency [63, 64] and is the most appropriate technology for the scale of MEMS devices [65, 66].

5.1 Piezoelectricity

Piezoelectric effect was reported by Jacques and Pierre Curie in 1880 [67, 68]. They found that some kind of crystals subjected to mechanical strain became electrically polarized. Furthermore, they found that the relationship between the degree of polarization and the applied strain is proportional. The inverse piezoelectric effect, these materials deform when a voltage is applied, was predicted by Lippmann [69] and confirmed experimentally by the brothers Curie.

Piezoelectric materials present an anisotropic behaviour. Consequently, the properties of the material depend upon the direction of the strain and the direction of the polarization, and in particular of the position of the electrodes. It is important to remark that the piezoelectric engineered materials, unlike natural materials, are subjected to a process called poling to impart the piezoelectric behaviour. The dipoles of the cells of a macroscopic crystalline structure are originally randomly oriented and the piezoelectric effect is negligible when the material is subjected to a mechanical stress. The poling process consist of applying a very high electric field that orients permanently the dipoles in the direction of the field, Figure 23.

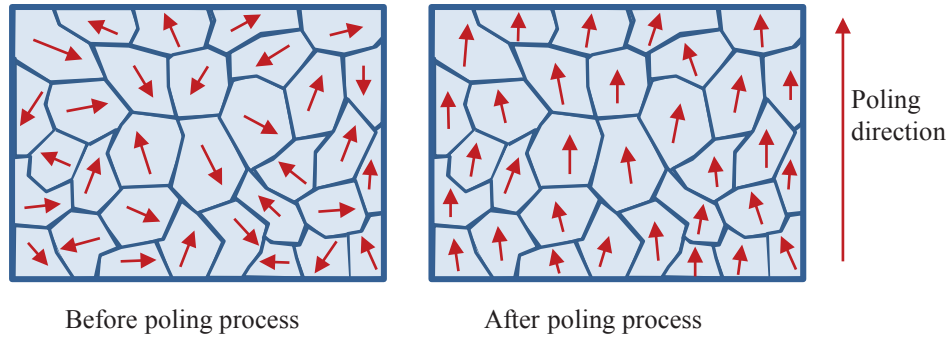


Fig. 23 The poling process induces piezoelectric properties in the material. Before the poling process the dipoles are randomly aligned (left). After poling process the dipoles tend to be pointed to poling direction (left)

It is important to avoid the depolarization of the piezoelectric material. There are two ways to de-pole a piezoelectric material: (i) applying a very high electric field opposite to the field applied during the poling process, and (ii) heating the material above its Curie temperature.

5.2 Properties of piezoelectric materials

The compliance, coupling and permittivity properties for a piezoelectric material are second order tensors due to the anisotropic behaviour of these materials. As a result, the constants defined to characterize the piezoelectric materials have two subscripts, one related to the applied force, stress, and the other related to change in length, the strain. The specific coordinate system used to indicate the directions of the stress and the strain are shown in Figure 24. Conventionally, the poling direction is the z-axis (or 3), except in quartz where it is x-axis (or 1).

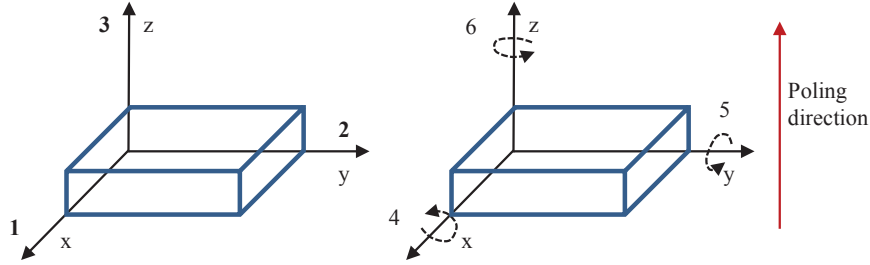


Fig. 24 Specific notation for coordinates used in piezoelectric constants and quantities. The z-axis coincides with the poling direction. The numbers 1,2 and 3 represent the Cartesian coordinates (left) and the numbers 4, 5 and 6 represents the shear about Cartesian coordinates (right).

As it can be seen, the x, y and z axes are represented by the subscripts 1, 2 and 3 respectively. The subscripts 4, 5 and 6 are used to represent the rotation about these axes.

The constants commonly used to characterize piezoelectric materials are: (i) the piezoelectric strain/charge constant, d , (ii) the piezoelectric stress/voltage constant, g , (iii) the electromechanical coupling coefficient, k , and (iii) the permittivity, ϵ .

The anisotropic piezoelectric mechanical and electrical quantities are linked using double subscripts (i.e. k_{ij}). The subscripts designate the axis parallel to the direction of the excitation and the axis parallel to the direction of the response [70].

The strain/charge constants, d_{ij} , express the relationship between the strain developed along or around an axis and the applied electric field parallel to an axis when all external stresses are constant [71]:

$$d_{ij} = \frac{\text{strain developed along } j - \text{axis}}{\text{applied electric field parallel to } i - \text{axis}} \quad \left(\frac{m}{V} \right) \quad (5)$$

The strain/charge constant can also be defined as the relationship between the short-circuit charge per unit area flowing between connected electrodes that are perpendicular to an axis and the stress applied along or around an axis when all other external stresses are constant [71]:

$$d_{ij} = \frac{\text{short-circuit charge flow perpendicular to } i\text{-axis}}{\text{applied stress along } j\text{-axis}} \quad \left(\frac{C}{N} \right) \quad (6)$$

The stress/voltage constant, g_{ij} , is the relationship between the open circuit field developed along an axis and the stress applied along or around an axis when all other external stresses are constant [71]:

$$g_{ij} = \frac{\text{open circuit field along } i\text{-axis}}{\text{stress applied along } j\text{-axis}} \quad \left(\frac{Vm}{N} \right) \quad (7)$$

The stress/voltage constant can also be defined as the relationship between the strain developed along an axis and the electric charge density applied to electrodes that are normal to an axis [71]:

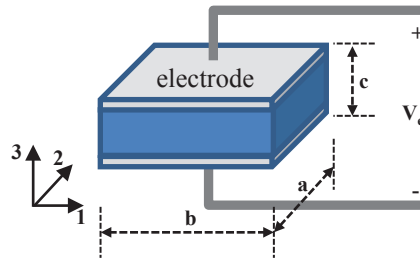
$$g_{ij} = \frac{\text{strain developed along } j\text{-axis}}{\text{applied charge density normal to } j\text{-axis}} \quad \left(\frac{m^2}{C} \right) \quad (8)$$

The electromechanical coupling coefficients, k_{ij} , are the energy ratios describing the conversion from mechanical energy to electrical energy or vice versa [64]. The ratio of energy stored, mechanical or electrical, to energy, mechanical or electrical, applied can be calculated squaring the electromechanical coupling factor, k^2 . The first subscript, i , indicates the direction of the electrical field and the second designates the direction of the mechanical strain. These coefficients have no dimensions. Equation 9 shows the relationship between the mechanical input energy in the j -axis, W_j^m , and the electrical energy stored in the i -axis, W_i^e .

$$k_{ij}^2 = \frac{W_i^e}{W_j^m} \quad (\text{dimensionless}) \quad (9)$$

The most common piezoelectric constants and coefficients used in energy harvesting systems are listed below using the dimensions and the reference system shown in Figure 25.

Fig. 25 Piezoelectric material with two electrodes on its opposite sides. V_e is the voltage across the electrodes and a , b and c are the dimensions of the piezoelectric element.



- d_{31} : This constant expresses the relation between the charge developed, Q , flowing between the shorted electrodes, $V_e = 0$ V, that are orthogonal to the poling

axis (3-z), and a force, F , applied along the axis 1. Therefore, the charge developed Q can be calculated using the equation 10, [72].

$$Q(V_e = 0V) = d_{31}F \frac{b}{c} \quad (10)$$

- d_{33} : This constant expresses the relation between the charge developed, Q , flowing between shorted electrodes that are orthogonal to the poling axis (3-z), and a force, F , applied in the direction of the polarization axis (3-z). Therefore, Q can be calculated using the equation 11, [72]:

$$Q(V_e = 0V) = d_{33}F \quad (11)$$

- g_{31} : This constant expresses the relationship between the induced electric field is along the poling axis(3-z) and the force applied in the direction orthogonal to the polarization axis (1-x), Figure 26. Therefore, the induced voltage can be calculated as [72]:

$$V_e(Q = 0C) = g_{31} \frac{F}{a} \quad (12)$$

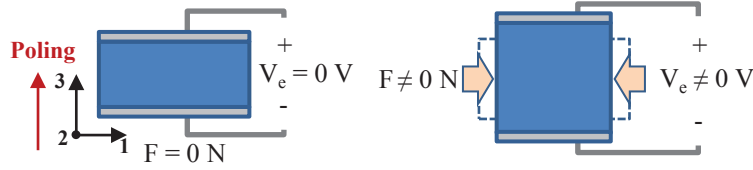


Fig. 26 The 31 mode operation for piezoelectric materials. No voltage is induced when no force is applied (left) and voltage is induced when force is applied (right)

- g_{33} : This constant expresses the relationship between the induced electric field along the poling axis(3-z) and the force applied in the direction of the polarization axis (3-z), Figure 27. Therefore, voltage induced can be calculated as [72]:

$$V_e(Q = 0C) = g_{33}F \frac{c}{ab} \quad (13)$$

Therefore, the spatial orientation of the materials is very important. It must be taken into account when a system is modelled, analysed or simulated.

5.3 Piezoelectric materials

Piezoelectric materials are used in a range of applications such as pressure sensing, data storage, mechanical actuation, ultrasonic wave generation and energy harvest-

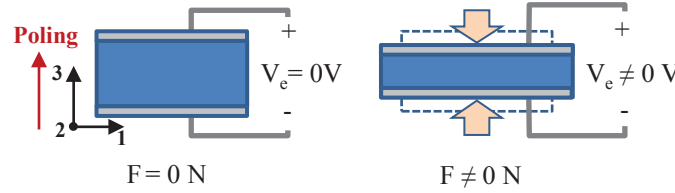


Fig. 27 The 33 mode operation for piezoelectric materials. Effect when no force is applied (left) and voltage is induced when force is applied along the poling axis (right)

ing. Owing to this wide range of application a large number of materials has been developed. The following classification includes the most available forms of this piezoelectric materials [73, 74]:

- Crystals: Quartz (SiO_2), Berlinite ($AlPO_4$), Gallium Orthophosphate $GaPO_4$, Turmaline, etc.
- Polycrystalline ceramics: Barium titanate ($BaTiO_3$), Lead Zirconate Titanate (PZT) [75]. These materials are characterized by its perovskite tungsten-bronze structure.
- Thin film non-ferroelectric materials: Sputtered zinc oxide (ZnO), Aluminium Nitride (AlN) [76].
- Polymeric materials: Polyvinylidene fluoride (PVDF) [77].
- Screen printable thick-films based upon piezoceramic powders [78] and composites such as polyvinylidene-trifluoroethylene-PZT (PVDF-TrFE) [79]
- Organic crystals: single-crystal diisopropylammonium chloride (DIPAC) and diisopropylammonium bromide (DIPAB) [80, 81]

MEMS devices require thin and thick film technologies since the layers of the materials must be below $100\text{ }\mu\text{m}$. Thin-film technologies, physical or chemical deposition, are used to fabricate films with thickness lower than $5\text{ }\mu\text{m}$. Thick layers with thickness up to $100\text{ }\mu\text{m}$ can be fabricated using the screen printing method. Maas et al. describes at [82] of printing PZT onto silicon, the powdered PZT is mixed with boro-silicate glass powder and an organic vehicle to make a paste, it is the ink. The layer is printed, dried to remove the solvent and finally fired. The aluminium nitride, AlN, has recently been incorporated to list of the materials used in energy harvesting. Schaijk et al. justify the selection of AlN as piezoelectric material since it is easy to process than PZT [83]. The piezoelectric constants of PZT are better than AlN but the main advantage of AlN is its compatibility with CMOS processing. This is because it is foreseeable in the near future new investigation will result in better performance devices based on AlN. Finally, the piezoelectric constants for common materials used in MEMS devices are shown in table 1.

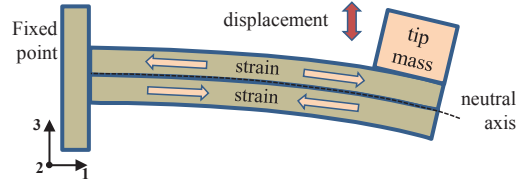
Table 1 Coefficients of common piezoelectric materials [64, 84, 85, 86].

Property	PZT-5H	PZT-5A	BaTiO ₃	PVDF	AlN	GaN	ZnO
d_{33} (10^{-12} C N $^{-1}$)	593	374	149	-33	5	3.7	12.4
d_{31} (10^{-12} C N $^{-1}$)	-274	-171	78	23	-2	-1.9	-5
g_{33} (10^{-3} V m N $^{-1}$)	19.7	24.8	14.1	330	-	-	-
g_{31} (10^{-3} V m N $^{-1}$)	-9.1	-11.4	5	216	-	-	-
k_{33} (dimensionless)	0.75	0.71	0.48	0.15	0.23	-	0.48
k_{31} (dimensionless)	0.39	0.31	0.21	0.12	-	-	0.182

5.4 Piezoelectric energy harvester

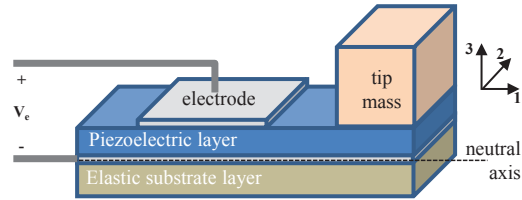
Energy harvesting MEMS devices based on piezoelectric materials generally have the cantilever beam structure shown in Figure 28. The beam is clamped at one end and the mechanical vibrations are generated principally along the 3rd axis through bending. As it can be seen, the vertical movement of the mass induces a strain along the x-axis (or 1). Accordingly, if a 31 mode piezoelectric material is deposited on the beam, then a voltage would be induced between the two sides of this material when it is exposed to vibration sources.

Fig. 28 Cantilever beam structure with a tip mass subjected to bending. The strain developed above the neutral axis is opposite to the strain developed below the neutral axis



The structure shown at figure 28 creates equal and opposite strains on the beam. Therefore, it is not possible to use a beam based only on a piezoelectric material as the total voltage or current generated would be null. To be effective as a generator a piezoelectric layer is fixed to a non-piezoelectric elastic layer, 29. Thereby the neutral axis, the line in which the beam do not change in length, is not in the center of the piezoelectric layer. This structure is named unimorph because it is composed of a unique piezoelectric active layer.

Fig. 29 The unimorph structure based on a piezoelectric layer and an inactive substrate. The generated voltage, V_e , depends only on the strain on the piezoelectric layer



The 33 mode of piezoelectric materials is often more favourable than 31 mode, see Table 1. It is a reason to use this mode but the structure shown at Figure 29 is not feasible since the direction of the induced electric field in 33 mode is parallel to the stress direction. The interdigitated electrode, IDE, configuration presented by Jeon et al at [66] and Park et al. at [87] enables to employ the 33 mode and discards the bottom electrode layer, Figure 30.

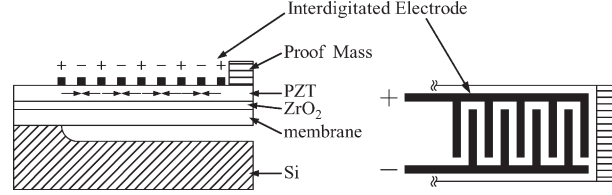


Fig. 30 Structure of the unimorph cantilevered beam with interdigitated electrode proposed by Jeon et al. [66]

IDE configuration has the additional advantage of allowing designer the adjustment of the electrode spacing and consequently output voltage since the open circuit voltage is proportional to the distance between electrodes, see equation 13. A comparison between the structures proposed to use the 31 and 33 modes can be found at Figure 31.

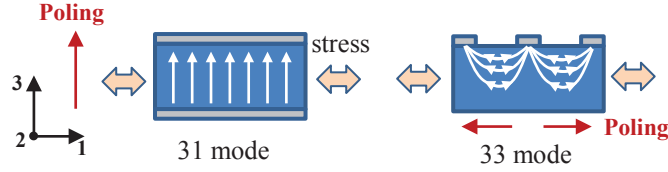


Fig. 31 Relationship between applied stress and induced field, white arrows, for 31 and 33 modes.

Therefore, the electrode lengths and shapes are important parameters that affect the output voltage due to the non uniformity of the strain along the beam [88]. Kim et al. have fabricated and compared piezoelectric energy harvesters based on d_{31} and d_{33} modes [89]. These authors have demonstrated that the output power of the d_{33} mode depends strongly on the dimensions of IDE.

5.4.1 Bimorph cantilever structure

The structure of a bimorph piezoelectric energy harvester based on a cantilever beam is shown in figure 32. Two piezoelectric layers are fixed to a non-piezoelectric elastic layer. The electrodes can be connected in series or in parallel configuration. The

main advantage of bimorph structure is that there is lower loss in mechanical support materials since only the piezoelectric layer is strained.

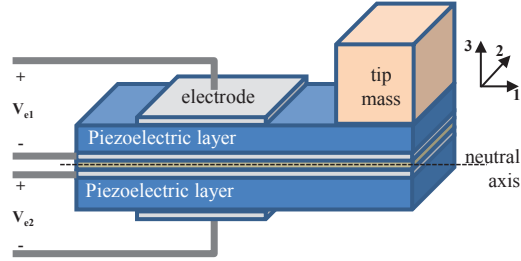


Fig. 32 Structure of a bimorph piezoelectric energy harvester

Currently, the optimization of the energy harvesters is one of the most important challenges due the low energy extracted. In order to analyse and optimize the designs, several models of the piezoelectric energy harvesters have been proposed. Lumped-parameter models allow simple expressions but with limited accuracy. Models based on distributed-parameter offers higher accuracy increasing the complexity of the expressions. Erturk et al. at [90] expose a detailed electromechanical modelling of piezoelectric energy harvesters.

5.4.2 Application example

A MEMS vibration energy harvester based on a PZT/PZT thick film bimorph with an integrated silicon tip mass is described in [91], Figure 33.

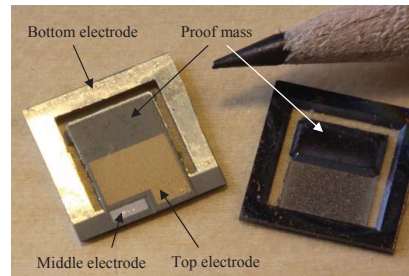


Fig. 33 Front and back of a MEMS-based PZT/PZT thick film bimorph vibration energy harvester fabricated by R. Xu et al [91]

The authors propose a new fabrication process that improves the quality of the thick film. The PZT layers are screen printed, treated with a high pressure process and finally sintered (high-temperature heating without melting the material). The characterization of the power output as a function of the acceleration is shown in Figure 34. The output power reaches $37.1 \mu\text{W}$ when the energy harvester is subjected to an acceleration of 1 g. It is important to denote that the power output due to the bottom layer and the power due to the top layer are very similar.

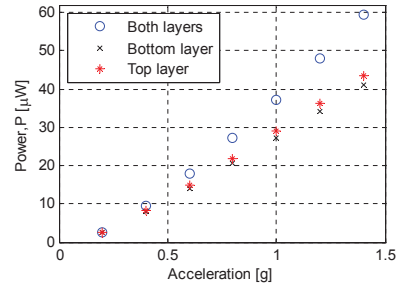


Fig. 34 RMS power output as a function of the input acceleration [91].

References

1. C. Liu, *Foundations of MEMS. Second Edition.* Pearson Education, 2012.
2. R. Ghodssi and P. Lin, *MEMS Materials and Processes Handbook.* Springer, 2012.
3. F. Laermer and A. Schilp, "Method for anisotropic plasma etching of substrates," 1996, US Patent 5,498,312.
4. —, "Method of anisotropic etching of silicon," 2003, US Patent 6,531,068.
5. K. S. Chen, A. A. Ayon, X. Zhang, and S. M. Spearing, "Effect of process parameters on the surface morphology and mechanical performance of silicon structures after deep reactive ion etching (DRIE)," *Microelectromechanical Systems, Journal of*, vol. 11, no. 3, pp. 264–275, Jun 2002.
6. S. Gorreta, D. Fernandez, E. Blokhina, J. Pons-Nin, V. Jimenez, D. O'Connell, O. Feely, J. Madrenas, and M. Dominguez, "Pulsed digital oscillators for electrostatic MEMS," *Circuits and Systems I: Regular Papers, IEEE Trans. on*, 2012.
7. R. T. Howe and R. S. Muller, "Polycrystalline silicon micromechanical beams," *Journal of The Electrochemical Society*, vol. 130, no. 6, pp. 1420–1423, 1983.
8. J. M. Bustillo, R. T. Howe, and R. S. Muller, "Surface micromachining for microelectromechanical systems," *Proceedings of the IEEE*, vol. 86, no. 8, pp. 1552–1574, Aug 1998.
9. <http://www.memscap.com/products/mumps>.
10. http://www.mems.sandia.gov/tech-info/summit_v.html.
11. <http://www.invensense.com/nfshuttle>.
12. <https://www.teledynedalsa.com/semi/fab/services/shuttleruns>.
13. <http://www.lionixbv.nl/mpw.html>.
14. A. Cowen, G. Hames, K. Glukh, and B. Hardy, *PiezoMUMPs Design Handbook. Revision 1.2*, MEMSCAP Inc., 2013.
15. J. Pons, S. Gorreta, E. Blokhina, D. O'Connell, O. Feely, and M. Domínguez, "Design and test of resonators using piezoMUMPS technology," in *Symposium on Design, Test, Integration and Packaging of MEMS / MOEMS (DTIP 2014)*, Cannes, France, april 1–4 2014.
16. B. Andò, S. Baglio, C. Trigona, N. Dumas, L. Latorre, and P. Nouet, "Nonlinear mechanism in mems devices for energy harvesting applications," *Journal of Micromechanics and Microengineering*, vol. 20, no. 12, p. 125020, 2010. [Online]. Available: <http://stacks.iop.org/0960-1317/20/i=12/a=125020>
17. S. Guan and B. Nelson, "Magnetic composite electroplating for depositing micromagnets," *Microelectromechanical Systems, Journal of*, vol. 15, no. 2, pp. 330–337, April 2006.
18. F. Cottone, H. Vocca, and L. Gammaitoni, "Nonlinear energy harvesting," *Phys. Rev. Lett.*, vol. 102, p. 080601, Feb 2009. [Online]. Available: <http://link.aps.org/doi/10.1103/PhysRevLett.102.080601>
19. B. Ando, S. Baglio, G. L'Episcopo, and C. Trigona, "Investigation on mechanically bistable mems devices for energy harvesting from vibrations," *Microelectromechanical Systems, Journal of*, vol. 21, no. 4, pp. 779–790, Aug 2012.

20. N. V. Myung, D.-Y. Park, B.-Y. Yoo, and P. T. Sumodjo, "Development of electroplated magnetic materials for {MEMS}," *Journal of Magnetism and Magnetic Materials*, vol. 265, no. 2, pp. 189 – 198, 2003. [Online]. Available: <http://www.sciencedirect.com/science/article/pii/S0304885303002646>
21. M. Han, Q. Yuan, X. Sun, and H. Zhang, "Design and fabrication of integrated magnetic mems energy harvester for low frequency applications," *Microelectromechanical Systems, Journal of*, vol. 23, no. 1, pp. 204–212, Feb 2014.
22. X. Sun, Q. Yuan, D. Fang, and H. Zhang, "Electrodeposition and characterization of conimnp permanent magnet arrays for {MEMS} sensors and actuators," *Sensors and Actuators A: Physical*, vol. 188, no. 0, pp. 190 – 197, 2012, selected papers from The 16th International Conference on Solid-State Sensors, Actuators and Microsystems. [Online]. Available: <http://www.sciencedirect.com/science/article/pii/S0924424711007394>
23. J. Qiu, J. Lang, and A. Slocum, "A curved-beam bistable mechanism," *Microelectromechanical Systems, Journal of*, vol. 13, no. 2, pp. 137–146, April 2004.
24. M. Saif, "On a tunable bistable mems-theory and experiment," *Microelectromechanical Systems, Journal of*, vol. 9, no. 2, pp. 157–170, June 2000.
25. M. Hoffmann, P. Kopka, and E. Voges, "All-silicon bistable micromechanical fiber switch based on advanced bulk micromachining," *Selected Topics in Quantum Electronics, IEEE Journal of*, vol. 5, no. 1, pp. 46–51, Jan 1999.
26. J. Casals-Terre, A. Fargas-Marques, and A. Shkel, "Snap-action bistable micromechanisms actuated by nonlinear resonance," *Microelectromechanical Systems, Journal of*, vol. 17, no. 5, pp. 1082–1093, Oct 2008.
27. S. Park and D. Hah, "Pre-shaped buckled-beam actuators: Theory and experiments," *Sensors and Actuators A: Physical*, vol. 148, no. 1, pp. 186 – 192, 2008. [Online]. Available: <http://www.sciencedirect.com/science/article/pii/S0924424708004056>
28. S. Krylov, B. R. Ilic, D. Schreiber, S. Seretensky, and H. Craighead, "The pull-in behavior of electrostatically actuated bistable microstructures," *Journal of Micromechanics and Microengineering*, vol. 18, no. 5, p. 055026, 2008. [Online]. Available: <http://stacks.iop.org/0960-1317/18/i=5/a=055026>
29. K. Das and R. C. Batra, "Pull-in and snap-through instabilities in transient deformations of microelectromechanical systems," *Journal of Micromechanics and Microengineering*, vol. 19, no. 3, p. 035008, 2009. [Online]. Available: <http://stacks.iop.org/0960-1317/19/i=3/a=035008>
30. B. Marinkovic and H. Koser, "Smart sand—a wide bandwidth vibration energy harvesting platform," *Applied Physics Letters*, vol. 94, no. 10, pp. –, 2009. [Online]. Available: <http://scitation.aip.org/content/aip/journal/apl/94/10/10.1063/1.3097207>
31. M. Marzencki, M. Defosseux, and S. Basrour, "Mems vibration energy harvesting devices with passive resonance frequency adaptation capability," *Microelectromechanical Systems, Journal of*, vol. 18, no. 6, pp. 1444–1453, Dec 2009.
32. D. S. Nguyen, E. Halvorsen, G. U. Jensen, and A. Vogl, "Fabrication and characterization of a wideband mems energy harvester utilizing nonlinear springs," *Journal of Micromechanics and Microengineering*, vol. 20, no. 12, p. 125009, 2010. [Online]. Available: <http://stacks.iop.org/0960-1317/20/i=12/a=125009>
33. S. Nguyen and E. Halvorsen, "Nonlinear springs for bandwidth-tolerant vibration energy harvesting," *Microelectromechanical Systems, Journal of*, vol. 20, no. 6, pp. 1225–1227, Dec 2011.
34. A. Elshurafa, K. Khirallah, H. Tawfik, A. Emira, A. Abdel Aziz, and S. Sedky, "Nonlinear dynamics of spring softening and hardening in folded-mems comb drive resonators," *Microelectromechanical Systems, Journal of*, vol. 20, no. 4, pp. 943–958, Aug 2011.
35. L. Gabbay and S. Senturia, "Computer-aided generation of nonlinear reduced-order dynamic macromodels. i. non-stress-stiffened case," *Microelectromechanical Systems, Journal of*, vol. 9, no. 2, pp. 262–269, June 2000.
36. J. Mehner, L. Gabbay, and S. Senturia, "Computer-aided generation of nonlinear reduced-order dynamic macromodels. ii. stress-stiffened case," *Microelectromechanical Systems, Journal of*, vol. 9, no. 2, pp. 270–278, June 2000.

37. A. Hajati and S.-G. Kim, "Ultra-wide bandwidth piezoelectric energy harvesting," *Applied Physics Letters*, vol. 99, no. 8, pp. —, 2011. [Online]. Available: <http://scitation.aip.org/content/aip/journal/apl/99/8/10.1063/1.3629551>
38. L. Tvedt, D. S. Nguyen, and E. Halvorsen, "Nonlinear behavior of an electrostatic energy harvester under wide- and narrowband excitation," *Microelectromechanical Systems, Journal of*, vol. 19, no. 2, pp. 305–316, April 2010.
39. M. Umeda, K. Nakamura, and S. Ueha, "Analysis of the transformation of mechanical impact energy to electric energy using piezoelectric vibrator," *Japanese Journal of Applied Physics*, vol. 35, no. Part 1, No. 5B, pp. 3267–3273, 1996. [Online]. Available: <http://jjap.jsap.jp/link?JJAP/35/3267/>
40. M. Domínguez, J. Pons-Nin, and J. Ricart, "General dynamics of pulsed digital oscillators," *Circuits and Systems I: Regular Papers, IEEE Transactions on*, vol. 55, no. 7, pp. 2038–2050, Aug 2008.
41. E. Blokhina, J. Pons, J. Ricart, O. Feely, and M. Domínguez-Pumar, "Control of mems vibration modes with pulsed digital oscillators part i: Theory," *Circuits and Systems I: Regular Papers, IEEE Transactions on*, vol. 57, no. 8, pp. 1865–1878, Aug 2010.
42. J. Ricart, J. Pons-Nin, E. Blokhina, S. Gorreta, J. Hernando, T. Manzanque, J. Sanchez-Rojas, O. Feely, and M. Domínguez-Pumar, "Control of mems vibration modes with pulsed digital oscillators part ii: Simulation and experimental results," *Circuits and Systems I: Regular Papers, IEEE Transactions on*, vol. 57, no. 8, pp. 1879–1890, Aug 2010.
43. H. Liu, C. Lee, T. Kobayashi, C. J. Tay, and C. Quan, "Piezoelectric mems-based wideband energy harvesting systems using a frequency-up-conversion cantilever stopper," *Sensors and Actuators A: Physical*, vol. 186, no. 0, pp. 242 – 248, 2012, selected Papers presented at Eurosensors {XXV} Athens, Greece, 4-7 September 2011. [Online]. Available: <http://www.sciencedirect.com/science/article/pii/S092442471200057X>
44. —, "Investigation of a mems piezoelectric energy harvester system with a frequency-widened-bandwidth mechanism introduced by mechanical stoppers," *Smart Materials and Structures*, vol. 21, no. 3, p. 035005, 2012. [Online]. Available: <http://stacks.iop.org/0964-1726/21/i=3/a=035005>
45. H. Liu, C. J. Tay, C. Quan, T. Kobayashi, and C. Lee, "Piezoelectric mems energy harvester for low-frequency vibrations with wideband operation range and steadily increased output power," *Microelectromechanical Systems, Journal of*, vol. 20, no. 5, pp. 1131–1142, Oct 2011.
46. W. Ma, R. Zhu, L. Rufer, Y. Zohar, and M. Wong, "An integrated floating-electrode electric microgenerator," *Microelectromechanical Systems, Journal of*, vol. 16, no. 1, pp. 29–37, Feb 2007.
47. M. Ahmad, M. M. Khir, and J. Dennis, "Design and modeling of the trapezoidal electrodes array for electrets energy harvester," in *SPIE Defense, Security, and Sensing*. International Society for Optics and Photonics, 2013, pp. 87 280Z–87 280Z.
48. Y. Suzuki, M. Edamoto, N. Kasagi, K. Kashiwagi, Y. Morizawa, T. Yokoyama, T. Seki, and M. Oba, "Micro electret energy harvesting device with analogue impedance conversion circuit," in *PowerMEMS 2008*, 2008, pp. 7 – 10.
49. P. Basset, D. Galayko, A. M. Paracha, F. Marty, A. Dudka, and T. Bourouina, "A batch-fabricated and electret-free silicon electrostatic vibration energy harvester," *Journal of Micromechanics and Microengineering*, vol. 19, no. 11, p. 115025, 2009. [Online]. Available: <http://stacks.iop.org/0960-1317/19/i=11/a=115025>
50. Y. Suzuki, "Recent progress in mems electret generator for energy harvesting," *IEEJ Transactions on Electrical and Electronic Engineering*, vol. 6, no. 2, pp. 101–111, 2011. [Online]. Available: <http://dx.doi.org/10.1002/tee.20631>
51. T. T., "Life time of thermal electrets of carnauba wax, esters, fatty acids and alcohols," in *7th International Symposium on Electrets*, 1991, pp. 106 – 110.
52. T. Minami, T. Utsubo, T. Yamatani, T. Miyata, and Y. Ohbayashi, "Sio2 electret thin films prepared by various deposition methods," *Thin Solid Films*, vol. 426, no. 1–2, pp. 47 – 52, 2003. [Online]. Available: <http://www.sciencedirect.com/science/article/pii/S0040609002013020>

53. Y. Sakane, Y. Suzuki, and N. Kasagi, "The development of a high-performance perfluorinated polymer electret and its application to micro power generation," *Journal of Micromechanics and Microengineering*, vol. 18, no. 10, p. 104011, 2008. [Online]. Available: <http://stacks.iop.org/0960-1317/18/i=10/a=104011>
54. A. Nimo, U. Mescheder, B. Müller, and A. S. A. Elkeir, "3d capacitive vibrational micro harvester using isotropic charging of electrets deposited on vertical sidewalls," in *SPIE Microtechnologies*. International Society for Optics and Photonics, 2011, pp. 80 661Q–80 661Q.
55. U. Mescheder, B. Müller, S. Baborie, and P. Urbanovic, "Properties of sio 2 electret films charged by ion implantation for mems-based energy harvesting systems," *Journal of Micromechanics and Microengineering*, vol. 19, no. 9, p. 094003, 2009. [Online]. Available: <http://stacks.iop.org/0960-1317/19/i=9/a=094003>
56. U. Mescheder, A. Nimo, B. Müller, and A. Elkeir, "Micro harvester using isotropic charging of electrets deposited on vertical sidewalls for conversion of 3d vibrational energy," *Microsystem Technologies*, vol. 18, no. 7-8, pp. 931–943, 2012. [Online]. Available: <http://dx.doi.org/10.1007/s00542-011-1418-4>
57. E. Westby and E. Halvorsen, "Design and modeling of a patterned-electret-based energy harvester for tire pressure monitoring systems," *Mechatronics, IEEE/ASME Transactions on*, vol. 17, no. 5, pp. 995–1005, Oct 2012.
58. K. Yamashita, M. Honzumi, K. Hagiwara, Y. Iguchi, and Y. Suzuki, "Vibration-driven mems energy harvester with vertical electrets," *Proc. PowerMEMS*, pp. 165–168, 2010.
59. F. Wang and O. Hansen, "Electrostatic energy harvesting device with out-of-the-plane gap closing scheme," *Sensors and Actuators A: Physical*, no. 0, pp. –, 2014. [Online]. Available: <http://www.sciencedirect.com/science/article/pii/S0924424714000910>
60. H. Liu, K. How Koh, and C. Lee, "Ultra-wide frequency broadening mechanism for micro-scale electromagnetic energy harvester," *Applied Physics Letters*, vol. 104, no. 5, pp. –, 2014. [Online]. Available: <http://scitation.aip.org/content/aip/journal/apl/104/5/10.1063/1.4863565>
61. A. Marin, S. Bressers, and S. Priya, "Multiple cell configuration electromagnetic vibration energy harvester," *Journal of Physics D: Applied Physics*, vol. 44, no. 29, p. 295501, 2011. [Online]. Available: <http://stacks.iop.org/0022-3727/44/i=29/a=295501>
62. K. A. Cook-Chennault, N. Thambi, and A. M. Sastry, "Powering mems portable devices—a review of non-regenerative and regenerative power supply systems with special emphasis on piezoelectric energy harvesting systems," *Smart Materials and Structures*, vol. 17, no. 4, p. 043001, 2008. [Online]. Available: <http://stacks.iop.org/0964-1726/17/i=4/a=043001>
63. K. Morimoto, I. Kanno, K. Wasa, and H. Kotera, "High-efficiency piezoelectric energy harvesters of c-axis-oriented epitaxial pzt films transferred onto stainless steel cantilevers," *Sensors and Actuators A: Physical*, vol. 163, no. 1, pp. 428 – 432, 2010. [Online]. Available: <http://www.sciencedirect.com/science/article/pii/S0924424710003067>
64. S. Beeby, M. Tudor, and N. White, "Energy harvesting vibration sources for microsystems applications," *Measurement Science and Technology*, vol. 17, no. 12, pp. R175–R195, December 2006. [Online]. Available: <http://eprints.soton.ac.uk/263645/>
65. S.-G. Kim, S. Priya, and I. Kanno, "Piezoelectric mems for energy harvesting," *MRS Bulletin*, vol. 37, pp. 1039–1050, 2012. [Online]. Available: <http://hdl.handle.net/1721.1/75255>
66. Y. Jeon, R. Sood, J. h. Jeong, and S.-G. Kim, "Mems power generator with transverse mode thin film pzt," *Sensors and Actuators A: Physical*, vol. 122, no. 1, pp. 16 – 22, 2005. [Online]. Available: <http://www.sciencedirect.com/science/article/pii/S0924424705000683>
67. J. Curie and P. Curie, "Développement, par pression, de l'électricité polaire dans les cristaux hémiedres à faces inclinées," *Comptes Rendus des Séances de l'Academie des Sciences*, vol. 91, pp. 294–295, 1880.
68. —, "Sur l'électricité polaire dans les cristaux hémiedres à faces inclinées," *Comptes Rendus des Séances de l'Academie des Sciences*, vol. 91, pp. 383–386, 1880.
69. G. Lippmann, "Principe de la conservation de l'électricité, ou second principe de la théorie des phénomènes électriques," *J. Phys. Theor. Appl.*, vol. 10, no. 1, pp. 381–394, 1881. [Online]. Available: <http://dx.doi.org/10.1051/jphysap:0188100100038100>
70. "Ieee standard on piezoelectricity," *ANSI/IEEE Std 176-1987*, pp. 1–66, 1988.

71. D. Ensminger and F. Stulen, *Ultrasonics: Data, Equations and Their Practical Uses*. Taylor & Francis, 2008. [Online]. Available: <http://books.google.es/books?id=u2XIPFCbVPgC>
72. C. R. Bowen, H. A. Kim, P. M. Weaver, and S. Dunn, "Piezoelectric and ferroelectric materials and structures for energy harvesting applications," *Energy Environ. Sci.*, vol. 7, pp. 25–44, 2014. [Online]. Available: <http://dx.doi.org/10.1039/C3EE42454E>
73. G. H. Haertling, "Ferroelectric ceramics: History and technology," *Journal of the American Ceramic Society*, vol. 82, p. 797–818, 1999.
74. S. Beeby and N. White, *Energy Harvesting for Autonomous Systems*, ser. Artech House series smart materials, structures, and systems. Artech House, Incorporated, 2010. [Online]. Available: <http://books.google.co.uk/books?id=7H9xdFd4sikC>
75. B. Jaffe, R. S. Roth, and S. Marzullo, "Piezoelectric properties of lead zirconate-lead titanate solid-solution ceramics," *Journal of Applied Physics*, vol. 25, no. 6, 1954.
76. S. Trolier-McKinstry and P. Muralt, "Thin film piezoelectrics for mems," *Journal of Electroceramics*, vol. 12, no. 1-2, 2004.
77. A. J. Lovinger, "Ferroelectric polymers," *Science*, vol. 220, no. 4602, pp. 1115–1121, 1983. [Online]. Available: <http://www.sciencemag.org/content/220/4602/1115.abstract>
78. H. Baudry, "Screen printing piezoelectric devices," *Microelectronics International*, vol. 4, no. 3, pp. 71–74, 2013.
79. M. Dietze and M. Es-Souni, "Structural and functional properties of screen-printed pzt–pvdf–trfe composites," *Sensors and Actuators A: Physical*, vol. 143, no. 2, pp. 329 – 334, 2008. [Online]. Available: <http://www.sciencedirect.com/science/article/pii/S0924424707008771>
80. D.-W. Fu, W. Zhang, H.-L. Cai, J.-Z. Ge, Y. Zhang, and R.-G. Xiong, "Diisopropylammonium chloride: A ferroelectric organic salt with a high phase transition temperature and practical utilization level of spontaneous polarization," *Advanced Materials*, vol. 23, no. 47, pp. 5658–5662, 2011. [Online]. Available: <http://dx.doi.org/10.1002/adma.201102938>
81. D.-W. F. and Hong Ling Cai, Y. Liu, Q. Ye, W. Zhang, Y. Zhang, X.-Y. Chen, G. Giovannetti, M. Capone, J. Li, and R.-G. Xiong, "Diisopropylammonium bromide is a high-temperature molecular ferroelectric crystal," *Science*, vol. 339, no. 6118, pp. 425–428, 2013.
82. R. Maas, M. Koch, N. Harris, N. White, and A. Evans, "Thick-film printing of {PZT} onto silicon," *Materials Letters*, vol. 31, no. 1–2, pp. 109 – 112, 1997. [Online]. Available: <http://www.sciencedirect.com/science/article/pii/S0167577X96002492>
83. R. van Schaijk, R. Elfrink, T. M. Kamel, and M. Goedbloed, "Piezoelectric aln energy harvesters for wireless autonomous transducer solutions," in *Sensors, 2008 IEEE*, Oct 2008, pp. 45–48.
84. I. L. Guy, S. Muensit, and E. M. Goldys, "Extensional piezoelectric coefficients of gallium nitride and aluminum nitride," *Applied Physics Letters*, vol. 75, no. 26, 1999.
85. S. Tadigadapa and K. Mateti, "Piezoelectric mems sensors: state-of-the-art and perspectives," *Measurement Science and Technology*, vol. 20, no. 9, p. 092001, 2009. [Online]. Available: <http://stacks.iop.org/0957-0233/20/i=9/a=092001>
86. D. Crisler, J. Cupal, and A. Moore, "Dielectric, piezoelectric, and electromechanical coupling constants of zinc oxide crystals," *Proceedings of the IEEE*, vol. 56, no. 2, pp. 225–226, Feb 1968.
87. J. C. Park, J. Y. Park, and Y. Lee, "Modeling and characterization of piezoelectric d33-mode mems energy harvester," *Microelectromechanical Systems, Journal of*, vol. 19, no. 5, pp. 1215–1222, Oct 2010.
88. J. Cho, M. Anderson, R. Richards, D. Bahr, and C. Richards, "Optimization of electromechanical coupling for a thin-film pzt membrane: I. modeling," *Journal of Micromechanics and Microengineering*, vol. 15, no. 10, p. 1797, 2005. [Online]. Available: <http://stacks.iop.org/0960-1317/15/i=10/a=002>
89. S.-B. Kim, H. Park, S.-H. Kim, H. Wickle, J.-H. Park, and D.-J. Kim, "Comparison of mems pzt cantilevers based on d31 and d33 modes for vibration energy harvesting," *Microelectromechanical Systems, Journal of*, vol. 22, no. 1, pp. 26–33, Feb 2013.
90. A. Erturk and D. J. Inman, *Piezoelectric energy harvesting*. John Wiley & Sons, 2011.

91. R. Xu, A. Lei, C. Dahl-Petersen, K. Hansen, M. Guizzetti, K. Birkelund, E. Thomsen, , and O. Hansen, "Fabrication and characterization of mems-based pzt/pzt bimorph thick film vibration energy harvesters," *Journal of Micromechanics and Microengineering*, vol. 22, no. 9, 2012.